A meso-scale simulation framework for predicting the mechanical response of triaxial braided composites

Tobias Wehrkamp-Richter[a,c,*], Nelson V. De Carvalho[b], Silvestre T. Pinho[c]

[a] *Institute for Carbon Composites, Technische Universität München, Faculty for Mechanical Engineering, Boltzmannstr. 15, D-85748 Garching b. München, Germany*
[b] *National Institute of Aerospace, resident at: Durability, Damage Tolerance and Reliability Branch, NASA Langley Research Center, Hampton, VA 23681-2199, USA*
[c] *Department of Aeronautics, Imperial College London, SW7 2AZ London, United Kingdom*

Abstract

In this paper, we propose a novel simulation framework for accurately predicting the mechanical response of highly compacted triaxial braided composites using meso-scale finite element models. Unit cells with a realistic internal geometry are generated within an automated simulation work-flow. Local volumetric interpenetrations are removed from a nominal geometry in a fictitious thermal simulation step. A compaction simulation of a single textile layer is performed to the desired target fibre volume fraction while implicitly considering multiple plies in different nesting configurations through periodic boundary conditions. For mechanical simulation, a matrix pocket mesh is created from a reconstruction of the deformed textile. A novel meshing methodology incorporates branching cohesive yarn-to-yarn and yarn-to matrix interfaces for modelling delamination. The framework was validated by detailed comparison with experimental results for three braid architectures. The excellent correlation of the internal geometry and the elastic properties underlines the framework's potential for future damage modelling.

Keywords: A. Fabrics/textiles; C. Computational modelling; E. Braiding; Unit cell

---

1. Introduction

Braiding combines an automated and reproducible process together with an excellent rate of material deposition for mass-production of high performance structures [1]. Accurately modelling the mechanical response of 2D braided composites, however, remains a challenging task due to their textile nature, which includes out-of-plane waviness, interactions between intertwining bundles and nesting of multiple plies in the through-thickness direction. Numerical modelling using meso-scale finite-element (FE) unit cell models provides a powerful tool to study the material behaviour of braided composites. Typically, a representative domain of the internal textile geometry is considered, wherein the constituent reinforcing yarns are explicitly modelled as solid continua. This approach can be applied to a variety of problems, ranging from determining dry fabric permeability or draping characteristics to the composite mechanical response, including the prediction of stress-strain fields, macroscopic mechanical properties, and the investigation of the non-linear behaviour with damage initiation and development.

The fidelity of unit cell models is largely affected by a realistic representation of the underlying textile geometry. Geometry pre-processors, such as WiseTex [2] or TexGen [3] provide good results for a variety of textile architectures, but modelling highly compacted triaxial braided composites with global fibre volume fractions (FVFs) of $55 - 60\%$

---

[*] Corresponding author: wehrkamp-richter@lcc.mw.tum.de; tel. +49 89 289 10433; fax. +49 89 289 15097

remains challenging. Here, the non-orthogonal interlacing of three in-plane fibre directions yields a complex internal geometry. After compacting multiple textile layers, the fabric features severely distorted yarns with multiple contact zones, locally varying intra-yarn FVF and fibre orientations.

Recently, increased research emphasis has been put on extending established textile modelling strategies [4] to more realistic geometry models [5]. Hivet and Boisse [6] developed a consistent 3D CAD formulation devoid of interpenetrations for the forming simulation of 2D woven fabrics in which contact zones between yarns are represented by shared geometrical faces. Using a hypoelastic material model for the yarns, the compaction and nesting behaviour of stacked 2D woven fabrics was investigated by [7]. In addition, Grail et al. [8] developed a mesh distortion algorithm to remove the resulting mesh inconsistency between orthogonal yarns after forming and investigated the mechanical performance of the resulting composite unit cell. Other researcher have tried to mimic the dry fabric behaviour by representing each bundle through several chains of one-dimensional finite elements in contact, thus explicitly rendering the effect of inter-fibre sliding [9, 10]. While results of the investigated 3D woven geometry agree well with microcomputed tomography (μCT) scans, a sophisticated post-processing technique is necessary to reconstruct yarn surfaces and generate a volumetric mesh for further mechanical analysis. Additionally, the multitude of contacts in the model is accompanied by a high computational expense and limits the degree of model parallelisation. Green et al. [11] studied the mechanical response of the above mentioned geometry using FE voxel discretisation and found significant differences between nominal and deformed geometry. Further studies on voxel modelling of textile composites [12, 13] concluded that although the elastic properties are in good agreement with a conventional mesh discretisation, the potential for simulating damage initiation and propagation is limited due to artificial stress concentrations induced by the staircase-like representation of the geometry. Additionally, the inadequate representation of the yarn interfaces impedes the possibility to model delamination in the unit cell. Another approach for obtaining a representative geometry model is the direct reconstruction of image data. Compared to a nominal geometry model, Naouar et al. [14] obtained an improved correlation with forming experiments of a single layer of dry woven fabric obtained from μCT images. Faes et al. [15] created a detailed 2D representative volume element (RVE) model of microscopic images taken from polished specimen edges to study the stress distribution in multiple nested layers. Considering the high geometrical characterisation effort for a single localised geometry, these inverse modelling approaches provide only limited capabilities for predicting the mechanical response of multiple textile architectures. In the presented work, the authors propose a modelling framework for predicting the mechanical response of triaxial braided composites using mesoscopic FE unit cells with a realistic internal geometry. The general procedure and the outline of the framework are derived from a list of key modelling requirements condensed from the previously mentioned literature:

1. Increased computational efficiency or modelling detail by
    - minimisation of the simulation domain through the use of reduced unit cell (rUCs) models and application of advanced in-plane periodic boundary conditions (PBCs) [16, 17]
    - implicit consideration of nesting and stacking effects in a single layer model through out-of-plane PBCs during an explicit compaction simulation to obtain highly compacted textile architectures
2. Accurate representation of the textile geometry, interface and properties without unsound assumptions by
    - an interpenetration-free geometry model without over-idealisations [18]
    - an improved representation of the yarn-to-yarn and yarn-to-matrix interface without the need of introducing and artificial matrix layer [19–22]

    - correct representation of the global FVF through a realistic axial and braid intra-yarn FVF [8, 23, 24]

3. High fidelity in the prediction of the non-linear mechanical response by
    - the capability to capture typical failure modes encountered in the yarns, in the matrix pockets, and at their respective interface [23]
    - a high quality structured hexahedral mesh in the yarns for accurate predictions of stress-strain fields suitable for the application of 3D continuum damage models [25]
    - a matrix mesh without severely distorted tetrahedral elements
4. High degree of automation in model generation through
    - scripting for objectivity and easy accessibility to other users
    - relying on software packages widely used and available within the research community. Throughout this work, all models are generated and solved in the unified FE package Abaqus controlled by MATLAB and the Abaqus Python scripting API [26].

This paper is structured as follows: in Section 2, the meso-scale modelling framework is introduced. The four key steps implemented in the simulation work-flow are outlined. From an initial idealised geometry model, a reduced unit cell domain is extracted, it's periodic boundary conditions are derived, and two subsequent process simulation steps are addressed, including the elimination of volumetric interpenetrations and the explicit compaction to the desired FVF. A novel algorithm for the generation of the complex matrix pocket mesh is introduced. In Section 3, the numerical model is validated against experimental data by comparing internal geometry features and elastic properties for three braid architectures. Finally, the capabilities and limitations of the modelling approach are discussed, highlighting possible future improvements.

2. Modelling framework

2.1. Roadmap and data flow

The modelling procedure is schematically shown in Fig. 1. Based on a reduced unit cell (rUC) concept to minimise computational expense [16], a compacted and interpenetration-free composite geometry is created within a three stage simulation process. In the first step, a nominal textile geometry is constructed from user-defined input parameters, such as braiding angle, yarn spacing and cross-sectional shape. As a result of the absence of initial contact between intertwining fibre bundles at this stage, local volumetric interpenetrations are resolved in a subsequent fictitious thermal step in which contact is established within the entire unit cell. In the subsequent compaction simulation step to the desired target FVF, flexible membranes which model the support of adjacent layers are added in through-thickness direction. By applying different sets of periodic boundary conditions to the latter, the compaction of multiple plies in different stacking and nesting configurations is implicitly considered at at reduced computational cost. This approach further enables us to render global FVFs of $55 - 60\%$ through intra-yarn FVFs obtained from experiments for the axial and braid bundles. Finally, the deformed hexahedral yarn mesh is used in a series of boolean operations to create a tetrahedral matrix pocket mesh with continuous yarn-to-yarn and yarn-to-matrix cohesive interfaces for modelling delaminations.

By obtaining the final geometry in a step-by-step approach, as opposed to inversely reconstructing geometry directly from μCT measurements [18], the overall robustness of the unit cell generation algorithm improves drastically for a

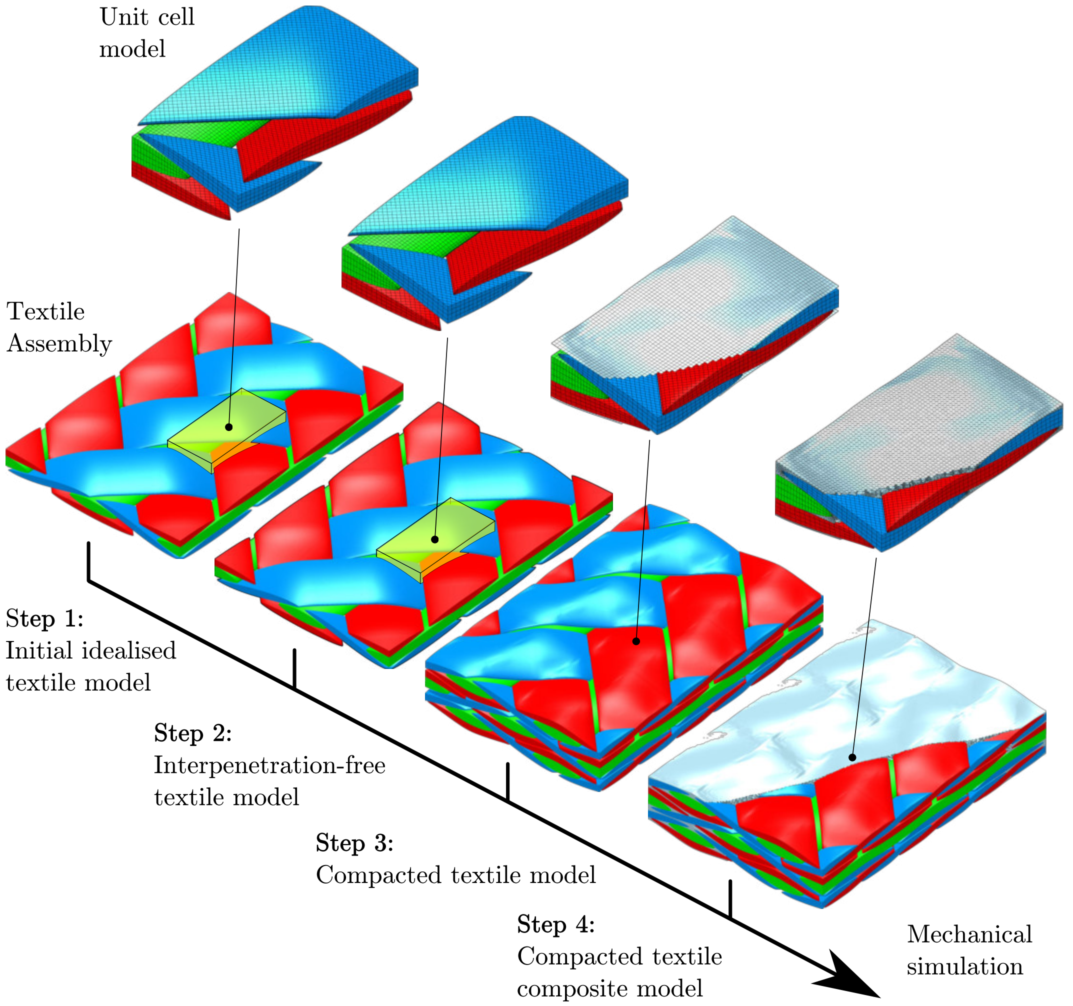

Figure 1: Roadmap and data flow for generating a realistic unit cell model

broader range of textile geometries. Instead of dealing with all the complexity of a compacted textile at once, the task is subdivided and accounted for by several simulation steps. While the interpenetration correction step takes care of any potential overlaps in the initial analytical geometry model, mostly independent of the geometry input by the user, the compaction step further ensures consistency of both the global target and intra-yarn FVFs. The frameworks high robustness is a key capability in order to cope with the large manufacturing variability in braided composites, where braiding angles in between 20° and 70° are commonly encountered across a typical component [27, 28].

2.2. Idealised geometry

In the step 1 of the framework, a surface mesh of the textile is generated from user-defined input parameters. Aside from the global braiding angle θ and the geometry of axial and bias bundles, including height, width, spacing and FE mesh size, their intra-yarn FVFs and the global target FVF are defined. Initially, a constant idealised cross-section is selected. Axial bundles indicated by the subscript a are assumed to be straight and their surface is described by a modified sinusoidal function

$$z_{\mathrm{a}} = \pm \frac{t_{\mathrm{a}}\,(1-\xi_{\mathrm{a}})}{2}\cos\left(\frac{y'_{\mathrm{a}}\,\pi}{w_{\mathrm{a}}}\right)^{n_{\mathrm{a}}} \pm \frac{\xi_{\mathrm{a}}\,t_{\mathrm{a}}}{2}, \quad \rightarrow \quad \text{cross-sectional term} \tag{1}$$

for which the required geometrical and global input parameters are displayed in Fig. 2, where the coordinate system $x_{\mathrm{a,b}}$,$y_{\mathrm{a,b}}$,$z_{\mathrm{a,b}}$ describes the master yarn surface and $x'_{\mathrm{a,b}}$,$y'_{\mathrm{a,b}}$,$z'_{\mathrm{a,b}}$ refers to the area centroid of a cross-section. The sign change indicates separate equations for the top and bottom surface. In a textile composite, the cross-sectional shape of a yarn is the product of the local preforming and compaction history and hence varies along its path. The sinusoidal term with a shape exponent n enables the generation of an adaptive cross-section capable of mimicking an arbitrary geometry through progressive morphing along its centre-line. Within an optimisation framework, it can also be used to minimise initial volumetric interpenetrations. Here, we exploit this geometrical degree of freedom to capture experimentally determined cross-sectional areas of bundles in addition to their width and height, such that consistency of FVF, fibre count and diameter are achieved. The effect of different magnitudes of the shape exponent n on the cross-sectional shape and area A for a typical yarn aspect ratio are highlighted in Fig. 3 (a) and (b), respectively. For $n = 1.0$, a nearly lenticular shape is reproduced, while the function closely resembles an ellipse with an exponent of $n = 0.5$. As n tends to zero, a rectangular cross-section with rounded corners is generated and the maximum area is achieved. For subsequent mesh quality purposes, the cross-section is truncated at a predefined side thickness of $\xi \cdot t$.

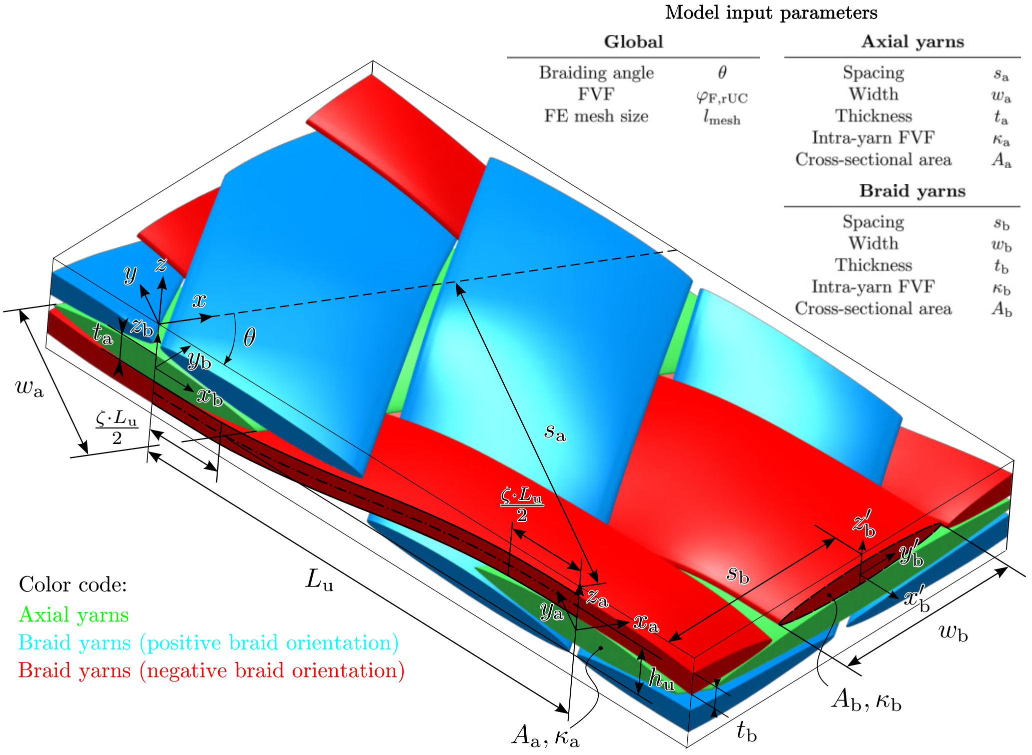

Model input parameters

Global	
Braiding angle	θ
FVF	$\varphi_{\mathrm{F,rUC}}$
FE mesh size	l_{mesh}

Axial yarns	
Spacing	s_{a}
Width	w_{a}
Thickness	t_{a}
Intra-yarn FVF	κ_{a}
Cross-sectional area	A_{a}

Braid yarns	
Spacing	s_{b}
Width	w_{b}
Thickness	t_{b}
Intra-yarn FVF	κ_{b}
Cross-sectional area	A_{b}

Figure 2: Initial geometry representation and model input data

For both the positively (b+) and negatively (b−) oriented braid yarn surfaces, an adapted formulation of the model developed for biaxial braids [29] is implemented. The total yarn path is assembled by a straight and an undulated segment. The latter is constructed by superimposing the cross-sectional term by an additional sinusoidal function responsible for the waviness of amplitude $h_{\mathrm{u}} = t_{\mathrm{a}} + t_{\mathrm{b}}$:

$$\begin{aligned} z_{\mathrm{b+,b-}}^{\mathrm{top,bottom}} &= \pm \frac{t_{\mathrm{b}}\,(1-\xi_{\mathrm{b}})}{2} \left|\cos\left(\frac{y'_{\mathrm{b}}\,\pi}{w_{\mathrm{b}}}\right)\right|^{n_{\mathrm{b}}} \pm \frac{\xi_{\mathrm{b}}\,t_{\mathrm{b}}}{2} \quad \rightarrow \quad \text{cross-sectional term} \\ &+ h_{\mathrm{u}} \sin\left(\frac{(x_{\mathrm{b}} - \omega_{\mathrm{b+,b-}})\,\pi}{L_{\mathrm{u}}\,(1-\zeta)}\right). \quad \rightarrow \quad \text{undulation term} \end{aligned} \tag{2}$$

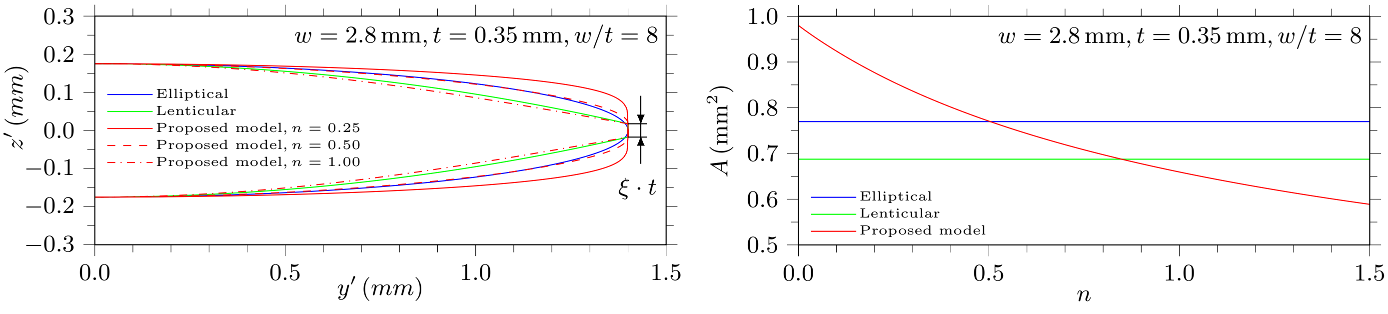

(a)

(b)

Figure 3: (a) Comparison of cross-sectional yarn shapes (b) Effect of shape exponent n on resultant area

The opposite signs in Equation 2 create the top and bottom master yarn surface. The straight undulation segment is obtained from:

$$\begin{aligned} z_{\mathrm{b+,b-}}^{\mathrm{top,bottom}} &= \pm \frac{t_{\mathrm{b}}\,(1-\xi_{\mathrm{b}})}{2} \left|\cos\left(\frac{y'_{\mathrm{b}}\,\pi}{w_{\mathrm{b}}}\right)\right|^{n_{\mathrm{b}}} \pm \frac{\xi_{\mathrm{b}}\,t_{\mathrm{b}}}{2} \quad \rightarrow \quad \text{cross-sectional term} \\ &+ h_{\mathrm{u}}\,\mathrm{sign}\left(\sin\left(\frac{x_{\mathrm{b}}\,\pi}{L_{\mathrm{u}}\,(1-\zeta)}\right)\right). \quad \rightarrow \quad \text{straight term} \end{aligned} \tag{3}$$

Both the positive and negative braid master yarn incorporate a braiding angle dependent localised phase shift given by

$$\omega_{\mathrm{b+,b-}} = \pm y'_{\mathrm{b}}\,\tan\left(\frac{\pi}{2} - 2\,\theta\right)\,\cos\left(\frac{x_{\mathrm{b}}\,\pi}{L_{\mathrm{u}}}\right)^2 \tag{4}$$

into the undulation term, the volumetric shape can be analytically distorted while retaining a constant cross-sectional area. A key advantage of this approach lies in the significant reduction of mutual braid yarn interpenetrations compared to a fixed cross-section for braiding angles ≠ 45°, as is exemplified for the non-orthogonal bundle intersections of a [0/±60] braid in Fig. 4 [29]. Each braid yarn is gradually distorted along its transverse direction by linearly increasing the phase shift. While the distortion term vanishes periodically at the intersection points of axial and braid yarns for minimised overlapping, it grows quadratically along the yarn path, until a maximum is reached at half of the wavelength L_{u}. Due to the closest proximity of braid yarns at their kinematic intersection point, the highest phase shift is introduced here.

It is worth mentioning that a pure rotation of cross-sections, as is often performed in woven composites [3], has shown only limited potential for an application in triaxial braids. In many cases, this procedure may reduce the interference with one entity on one side of a cross-section while causing a severe overlap on the opposite side. Since no in-plane waviness is considered in the bundles, the transverse position in each cross-section $y'_{\mathrm{a,b}}$ is coincident to its representation within the master yarn $y_{\mathrm{a,b}}$.

From the analytical surface description, an undulated master yarn is constructed in MATLAB through a series of blended cross-sections. Each cross-section is discretised symmetrically about its y' and z' axis with the user-defined FE mesh size which will later serve as a blueprint for the structured hexahedral unit cell mesh. Furthermore, several pieces along the master bundle are extracted and assembled in the desired textile pattern. Unlike in a periodic biaxial braid, the three interlacing fibre directions in a periodic triaxial braid induce a geometrical interdependency of the

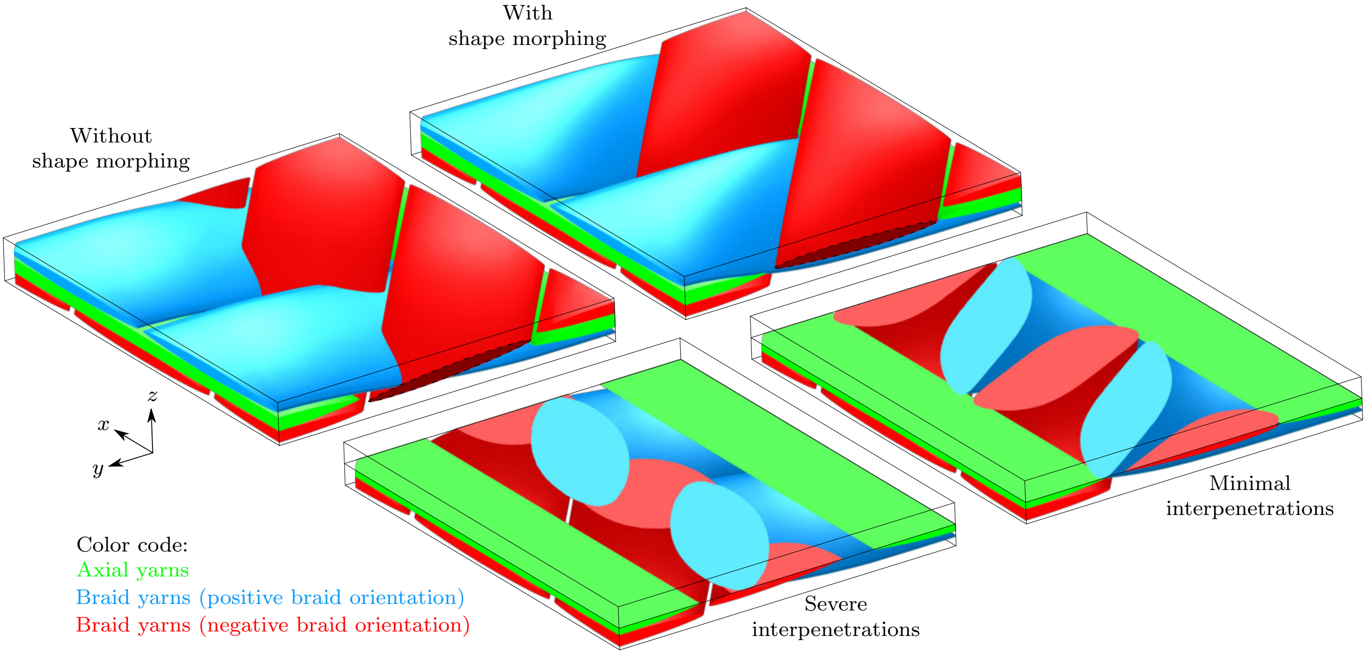

Figure 4: Effect of shape morphing on volumetric interpenetrations for [0/±60] braid

braiding angle θ, the axial yarn spacing s_a and the braid yarn spacing s_b for a given textile pattern, independent of the subsequent unit cell size and type. Out of these three parameters, only two can be chosen arbitrary. By satisfying the geometrical compatibility equation defined as

$$s_\mathrm{b} = s_\mathrm{a} \cos(\theta)\,, \tag{5}$$

a correct representation of cross-over points within a given braid undulation interval is ensured. Apart from restricting the yarn width to be equal or smaller than its corresponding spacing, there are no limitations on the geometry. In the last step, the assembled textile is rendered in 3D space. This allows a direct visual inspection of the geometry, an early detection of interpenetrations by geometric slicing and, if desired, a quick modification of parameters. Finally, an arbitrary unit cell shape can be selected for extraction.

2.3. Reduced unit cell domain and mesh generation

In order to minimise computational effort, a rUC for triaxial braided composites is derived on the basis of the equivalence framework for periodic structures [16] in Fig. 5. This approach allows us to reduce the modelling domain to a quarter of a smallest translational unit cell by exploiting internal symmetries of the textile topology. The width and height of the rUC are given by

$$w_\mathrm{rUC} = \frac{s_\mathrm{a}}{2} \quad ; \quad h_\mathrm{rUC} = \frac{s_\mathrm{b}}{\sin(\theta)}\,. \tag{6}$$

With the rUC dimensions defined and using spline interpolation along the fibre direction, the surface mesh is automatically converted into a solid CAD geometry. For the transverse direction, a linear interpolation based on the preceding symmetric discretisation of cross-sections is selected. This methodology enables us to retain the spatial information on predefined mesh seeds through geometric edges. By automatically creating a native Abaqus/CAE format with Python, any issues arising from external software import, such as imprecise geometry or unconnected faces are avoided. Hence,

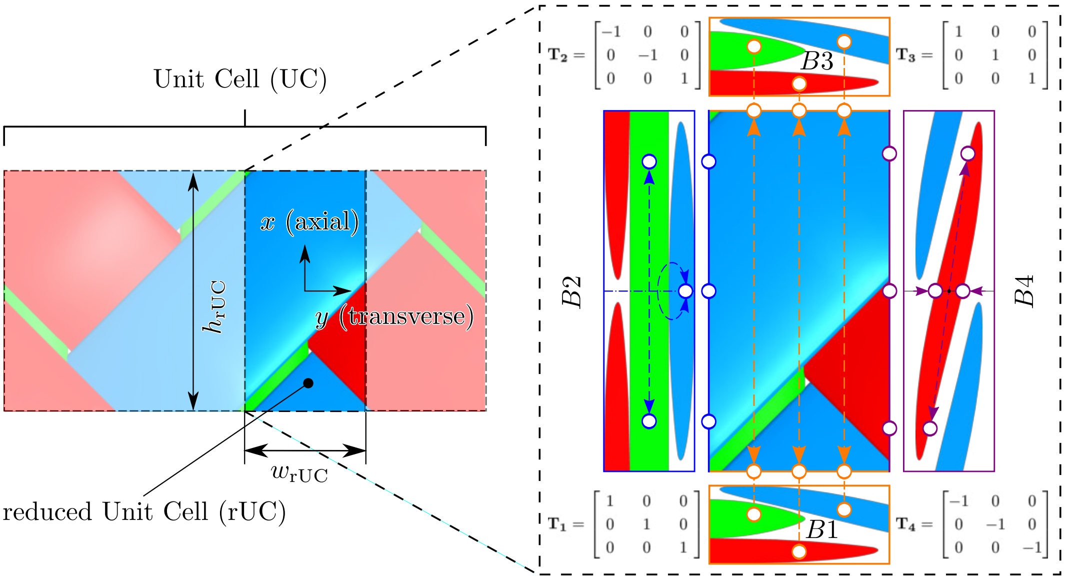

Figure 5: Reduced unit cell with periodic boundaries

a high robustness of the overall procedure is guaranteed. Working on CAD geometry as opposed to discrete meshes provides many key benefits, such as granting access to volumetric boolean operations that are particularly useful for mesoscopic modelling. For an arbitrary unit cell selected by the user, an exact CAD representation is obtained, independent of the angle of intersection between yarns and the periodic boundaries of the unit cell.

In light of the fact that a structured first-order hexahedral mesh provides an accurate solution at significantly less cost compared to a second-order tetrahedral mesh and the use of linear tetrahedral elements should be avoided as much as possible due their overly stiff behaviour [26], an automatic hexahedral meshing algorithm was developed for arbitrary yarn geometries.

A regular mesh is aligned with the fibre direction, as it offers many key advantages. Firstly, for a subsequent application of smeared crack models [30], crack bands may easily propagate along the fibre direction after strain localisation. Secondly, as a result of shape morphing, the fibre undulation varies not only along the yarn path, but also within each cross-section. Nevertheless, the local orientation tensor can be conveniently calculated on an element by element basis.

The biggest advantage of the presented approach, however, lies in the resulting inherent mesh periodicity caused by the boundary cut operation on the symmetric yarn discretisation. Geometric edges representing the transversal mesh seeds are cropped at the unit cell boundaries in a way that a periodic structure of boundary vertices is created, independent of the unit cell size or its type of periodicity. These anchor points highlighted in Fig. 6 are coincident with nodal positions and ensure the periodic nature of each boundary discretisation during the following mesh generation. The outcome of this initial step is depicted in Fig. 6 for a [0/±30] rUC. Now that all periodic boundaries are fully defined, the nodal positions inside the unit cell can be established. Depending on their relative position, length, and the number of periodic seed and target anchor points, each yarn is subdivided into logical meshing zones featuring up to two periodic boundaries. For single-sided periodic zones, e.g. zone 1 and zone 2, an orthogonal partition originating from each pair of seed anchor points produces a rectangular mesh pattern. Compatibility with the non-orthogonal boundary is satisfied by inserting single wedge elements per element row. In Fig. 6, zone 3 and 4 feature two periodic boundaries and hence must be treated separately. These two boundaries are subdivided into a target and a source

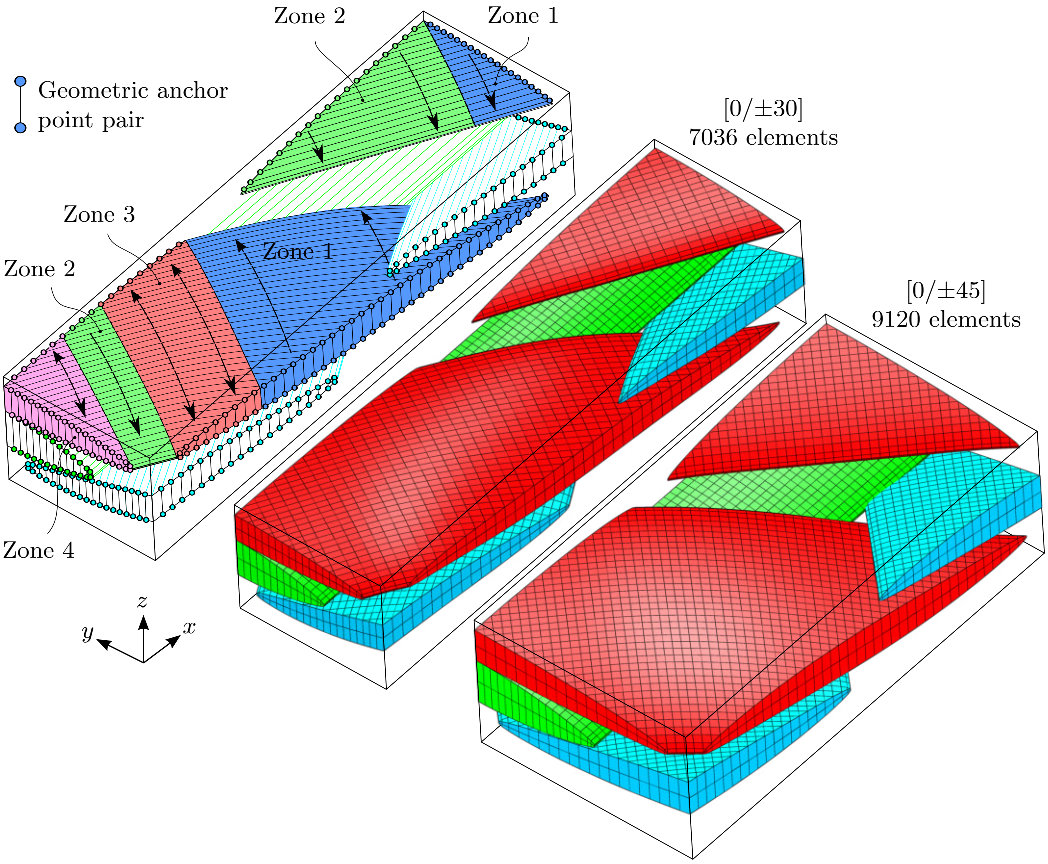

Figure 6: Meshing procedure and structured hexahedral mesh for [0/±30] and [0/±45] rUC, 40 elements per yarn width, 2 elements per yarn thickness, $\xi = 5\%$

side, with the latter determined by the minimum anchor point number. For each through-thickness pair of vertices positioned on the source side, a corresponding pair of target vertices is found, such that the aspect ratio of the mesh is optimised. By partitioning the yarns through a connection of these four corner points, the periodic boundaries remain unchanged. Finally, a user defined number of element rows is generated in through-thickness direction by a mere subdivision that preserves the periodic nature of the boundaries.

At the side edges of the bundles, the predefined thickness of $\xi \cdot t$ allows a compatible run-out of the hexahedral mesh. Here, the insertion of wedge elements was found to be disadvantageous, as they perform poorly in contact when large forces are introduced over a sharp edge in the fictitious thermal step. Additionally, the mesh is refined in close proximity to the side edges for optimised contact performance and element aspect ratio. An ideal choice for solid meshes with a high width to thickness aspect ratio are special purpose continuum elements with incompatible modes available in the commercial FE solver Abaqus [26]. In addition to the displacement degrees of freedom, incompatible deformation modes are added internally to improve the bending behaviour and eliminate parasitic shear locking. A slight increase in computational expense is nullified by the fact that significantly less elements are required in thickness direction leading in the consequence to an improved aspect ratio. While the meshing procedure was applied to the case of triaxial braided composites, it can be easily adapted to treat any kind of textile composite.

The periodic response is ensured by applying periodic displacement boundary conditions. Following the nomenclature of [16], they can be written for a deformable periodic body including arbitrary symmetries as

$$\mathbf{u}(A) - \gamma\,\mathbf{T}\,\mathbf{u}(\hat{A}) = -\left\langle\mathbf{F}\right\rangle\,\mathbf{T}\,\mathbf{x}^{\mathbf{O}\hat{\mathbf{E}}} \tag{7}$$

where $\mathbf{u}$ denotes the displacement field of equivalent points A and $\hat{A}$ at a periodic boundary. The coordinate transformation matrix $\mathbf{T}$ and the translation vector $\mathbf{x}^{\mathbf{O}\hat{\mathbf{E}}}$ define the tessellation of adjacent sub-domains, $\gamma = \pm 1$ describes their load reversal factor and $\langle\mathbf{F}\rangle$ is the volume averaged deformation gradient tensor. Considering the rUC shown in Fig. 5, the PBCs are implemented by enforcing a series of linear constraint equations between displacements of equivalent nodes on the previously created periodic boundary mesh. Following the procedure described in [16], a set of master equations for the in-plane boundaries is derived in Table 1 where $\langle\cdot\rangle$ denotes a volume-averaged variable. For edges and vertices sharing more than one periodic boundary, a system of linearly independent constraint equations is assembled.

Table 1: Master equations for implementation of in-plane periodic boundary conditions

$$\text{B1}\quad \begin{bmatrix} u_{\mathrm{x}}(h_{\mathrm{rUC}}/2, y, z) \\ u_{\mathrm{y}}(h_{\mathrm{rUC}}/2, y, z) \\ u_{\mathrm{z}}(h_{\mathrm{rUC}}/2, y, z) \end{bmatrix} - \begin{bmatrix} u_{\mathrm{x}}(-h_{\mathrm{rUC}}/2, y, z) \\ u_{\mathrm{y}}(-h_{\mathrm{rUC}}/2, y, z) \\ u_{\mathrm{z}}(-h_{\mathrm{rUC}}/2, y, z) \end{bmatrix} = \begin{bmatrix} \langle\varepsilon_{x}\rangle\ h_{\mathrm{rUC}} \\ \langle\varepsilon_{xy}\rangle\ h_{\mathrm{rUC}} \\ 0 \end{bmatrix}$$

$$\text{B2}\quad \begin{bmatrix} u_{\mathrm{x}}(-x, -w_{\mathrm{rUC}}/2, z) \\ u_{\mathrm{y}}(-x, -w_{\mathrm{rUC}}/2, z) \\ u_{\mathrm{z}}(-x, -w_{\mathrm{rUC}}/2, z) \end{bmatrix} - \begin{bmatrix} -u_{\mathrm{x}}(x, -w_{\mathrm{rUC}}/2, z) \\ -u_{\mathrm{y}}(x, -w_{\mathrm{rUC}}/2, z) \\ u_{\mathrm{z}}(x, -w_{\mathrm{rUC}}/2, z) \end{bmatrix} = \begin{bmatrix} -\langle\varepsilon_{xy}\rangle\ w_{\mathrm{rUC}} \\ -\langle\varepsilon_{y}\rangle\ w_{\mathrm{rUC}} \\ 0 \end{bmatrix}$$

$$\text{B3}\quad \begin{bmatrix} u_{\mathrm{x}}(-h_{\mathrm{rUC}}/2, y, z) \\ u_{\mathrm{y}}(-h_{\mathrm{rUC}}/2, y, z) \\ u_{\mathrm{z}}(-h_{\mathrm{rUC}}/2, y, z) \end{bmatrix} - \begin{bmatrix} u_{\mathrm{x}}(h_{\mathrm{rUC}}/2, y, z) \\ u_{\mathrm{y}}(h_{\mathrm{rUC}}/2, y, z) \\ u_{\mathrm{z}}(h_{\mathrm{rUC}}/2, y, z) \end{bmatrix} = \begin{bmatrix} -\langle\varepsilon_{x}\rangle\ h_{\mathrm{rUC}} \\ -\langle\varepsilon_{xy}\rangle\ h_{\mathrm{rUC}} \\ 0 \end{bmatrix}$$

$$\text{B4}\quad \begin{bmatrix} u_{\mathrm{x}}(-x, w_{\mathrm{rUC}}/2, -z) \\ u_{\mathrm{y}}(-x, w_{\mathrm{rUC}}/2, -z) \\ u_{\mathrm{z}}(-x, w_{\mathrm{rUC}}/2, -z) \end{bmatrix} + \begin{bmatrix} u_{\mathrm{x}}(x, w_{\mathrm{rUC}}/2, z) \\ u_{\mathrm{y}}(x, w_{\mathrm{rUC}}/2, z) \\ u_{\mathrm{z}}(x, w_{\mathrm{rUC}}/2, z) \end{bmatrix} = \begin{bmatrix} \langle\varepsilon_{xy}\rangle\ w_{\mathrm{rUC}} \\ \langle\varepsilon_{y}\rangle\ w_{\mathrm{rUC}} \\ 0 \end{bmatrix}$$

By exploiting the internal material symmetry at the periodic boundary B4 in Table 1, a symmetric undulation path about the z axis is implied throughout the subsequent simulation steps. In case additional geometrical features or defects are to be modelled, such as in-plane waviness, their shape and characteristic length must be comply with the symmetries at the rUC boundaries. In order to satisfy the admissibility of all sub-domains [16], homogenised in-plane shear $\langle\varepsilon_{xy}\rangle$ strains and out-of-plane shear $\langle\varepsilon_{xz}\rangle$ strains must be applied separately. Since the rUC can only be extracted at specific positions of the periodic textile, potential ply shifts in an explicit compaction simulation of multiple layers are restricted to integer multiples of half of the rUC width and height.

2.4. Interpenetration correction and compaction

With the sole geometric constraint that the yarn width cannot exceed its corresponding spacing, the initial idealised geometry directly represents the user input data. Although the degree of interpenetrations in the case of non-orthogonal interlacing can be minimised by using the previously described analytical formulation, there is no guarantee that any combination of input data will always yield an interpenetration free geometry model. In order to achieve a high robustness of the presented modelling framework for a large variety of textile geometries, potential volumetric interpenetrations are resolved by means of a fictitious explicit thermal disturbance step before the textile can be compacted to the desired FVF. The procedure is highlighted in Fig. 7. Initially, the rUC is subjected to a decrease in temperature accompanied by volumetric shrinkage of the yarns up to a point where all parts are distinctively separated. While the latter are subsequently reset to their initial temperature, they are now capable of interacting with each other by means of activated contact conditions. Considering the gradual expansion, a smooth transition into a compatible deformed geometric state is achieved. As this is a purely geometrical procedure of contraction and subsequent expansion, the constitutive law implemented is fictitious. An isotropic dummy material ($E = 20\,\text{GPa}$, $\nu = 0.45$) obtained from numerical sensitivity studies ensures an approximately constant bundle volume due to a quasi-incompressible material response without deteriorating the stable time increment in non-hybrid solid elements. Orthotropic coefficients of thermal expansion eliminate axial stretching ($\alpha_1 = 0,\ \alpha_2 = \alpha_3 = 1$), and a perfectly-plastic constitutive law with a von Mises yield criterion ($\sigma_{\text{yield}} = 250\,\text{MPa}$) allows local yielding at critical contact locations, in particular at the convergence point of axial, positive and negative braid yarn depicted in Fig. 7. Here, they are tightly interlocked, and this clinching effect can give rise to high localised contact penetrations. Aside from such critical locations, the yield stress is selected at such a level that most of the deformation remains elastic in order to avoid localised kinks in the yarns. With the applied strains eliminated in the in-plane PBC implementation, the rUC volume does not change during the simulation. Still, the periodic boundaries can deform freely, and geometrical coupling effects during the orthotropic contraction and expansion are averted.

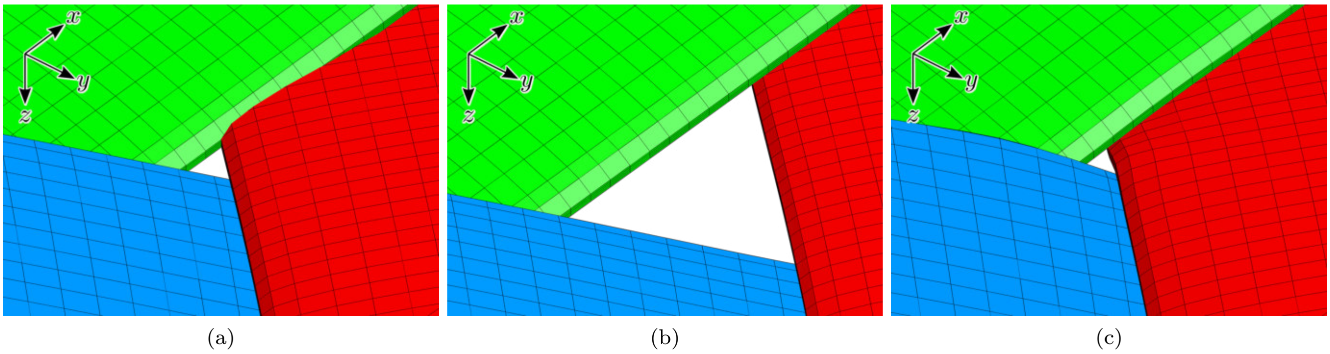

(a) (b) (c)

Figure 7: Resolving interpenetrations at the critical yarn convergence point (a) initial state (b) separation after contraction (c) interlock after expansion

A key feature of the presented work is the subsequent compaction simulation. Instead of explicitly modelling the forming process using a finite number of fabric layers in combination with a tool, we rely solely on the application of out-of-plane PBCs during an explicit compaction simulation of a single textile layer to further minimise computational effort. Flexible membranes of unit thickness which implicitly simulate the support of adjacent layers by means of PBCs are introduced on the top and bottom of the rUC. With the equivalence framework introduced previously, the effects of different nesting conditions such as ply shifting or flipping are studied by means of two stacking configurations shown in their compacted state in Fig. 8. The corresponding out-of-plane master equations are summarised in Table 2. As the membranes represent the support of adjacent layers, they comprise the material properties of the fibre bundles. Considering both the top and bottom cell assembled with a rotation of 180°about the z axis (flipped layer), axial fibre bundles of adjacent layers are positioned such that they are capable of closing large initial voids originating from the variable braid thickness. In this case of structural nesting described by [31], sections devoid of axial bundles are filled by their adjacent layer's equivalent. As a consequence, a rUC with locally varying thickness is produced. An identical nesting case can be obtained by incorporating a translational offset of w_{rUC} for the top and bottom rUC. However, a specific set of out-of-plane PBCs may not be chosen arbitrarily. Since rotational and mirror symmetries are exploited simultaneously in B2 and B4, the flipped top and bottom layers in Fig. 8 must be arranged inversely in order to satisfy the overall compatibility of the periodic structure. In the second nesting case, the plies are additionally shifted in axial (x) direction by a magnitude of $h_{\mathrm{rUC}}/2$. In contrast to the first nesting case, the braid bundles are now positioned directly on top of each other. Hence, regions of high packing densities are supplemented by local resin rich areas in the textile after compaction.

It is important to note that the purpose of the model at this stage is not to represent a dry fabric. The input parameters shown in Fig. 2 should be chosen to match the finished composite as closely as possible. Since we implicitly consider the yarn compaction behaviour by measuring the finished product rather than explicitly simulate the physical constitutive response of the dry fibre bundles, several localised deformation modes, such as yarn flattening, interactions with the tool, and the compaction force are not directly captured. Instead, we focus on quickly generating compacted unit cells for mechanical simulations by means of mimicking global compaction phenomena, such that any artificial scaling of intra-yarn FVF is avoided, The compaction step's primary mechanism comprises the shape distortion and repositioning of yarns due to mutual contact during compaction, such that large resin rich regions are closed and direct contact is established between individual fibre bundles. Finally, a more realistic geometry model of variable thickness enriched by a multitude of defects and imperfections is obtained, without the need of characterizing the complex mechanical behaviour of the dry fibre bundles. Nevertheless, the modular approach of the framework further allows for an additional implementation of physical compaction phenomena, for example by implementing a transversely-isotropic hypo-elastic constitutive law for the yarns [32, 33].

During the compaction operation, all yarn volumes V and hence intra-yarn FVFs κ remain approximately constant, enabling a priori determination of the average compacted ply thickness $\bar{t}_{\mathrm{rUC,c}}$ to achieve the global target FVF $\varphi_{\mathrm{F,rUC}}$:

$$\begin{aligned}\bar{t}_{\mathrm{rUC,c}} &= \frac{V_{\mathrm{a}}\,\kappa_{\mathrm{a}} + V_{\mathrm{b}}\,\kappa_{\mathrm{b}}}{4\,\varphi_{\mathrm{F,rUC}}\,h_{\mathrm{rUC}}\,w_{\mathrm{rUC}}} \\ &= \frac{h_{\mathrm{rUC}}\,A_{\mathrm{a}}\,\kappa_{\mathrm{a}} + 2\,L_{\mathrm{u'}}\,A_{\mathrm{b}}\,\kappa_{\mathrm{b}}}{2\,\varphi_{\mathrm{F,rUC}}\,h_{\mathrm{rUC}}\,w_{\mathrm{rUC}}}\end{aligned} \tag{8}$$

The yarn volumes V_{a} and V_{b} within the rUC are directly determined from the actual mesh discretisation, meaning that the target FVF is achieved independently of the element size. Further mesh refinement in order to obtain FVF convergence, as is commonly performed in voxel models [12], or a discretisation error due to mismatching geometry and mesh are eliminated. As the overall layer thickness gradually decreases over time, the global fibre volume fraction increases up to its target value. For a [0/±45] braid under investigation, the process is visualised using an assembly of several rUCs in Fig. 10. From the initial state at $\varphi_{\mathrm{F,rUC}} = 0.38$, the flat membranes are subjected to a prescribed displacement. Once interacting with the fabric, mutual deformations occur. Upon further compaction, they tend to locally accommodate to the underlying geometric shapes, thus increasing the contact area and the resulting compaction pressure. The final stage features a tightly packed structure of deformed bundles in direct contact. Here, the initially straight axial yarns exhibit a minor degree of crimp accompanied by a reduction in crimp in the braid yarns.

Considering that the assumption of a periodic stacking during the compaction process neglects a potential influence of rigid tool boundaries on the internal geometry of the outer layers, its applicability should be verified against the actual manufacturing process and the ply count of the braided component. In case of a severe impact of the tool on the yarn geometry, as in the case of laminates with few plies manufactured by resin transfer moulding (RTM), an explicit representation of the full stack and the tool may be necessary in order to capture their mutual mechanical interactions, such as flatting of the surface yarns [34]. For higher numbers of braided layers [35], however, or for vacuum infusion processes with a single-sided flexible membrane [36, 37], the advantages of drastically reducing computational expense can outweigh the loss in modelling detail.

Table 2: Out-of-plane PBC master equations

Nesting case 1: top ply: flipped, inverted; bottom ply: flipped

$$\text{B5}\quad \begin{bmatrix} u_\mathrm{x}(-x,-y,\bar{t}_\mathrm{rUC}/2) \\ u_\mathrm{y}(-x,-y,\bar{t}_\mathrm{rUC}/2) \\ u_\mathrm{z}(-x,-y,\bar{t}_\mathrm{rUC}/2) \end{bmatrix} + \begin{bmatrix} u_\mathrm{x}(x,y,\bar{t}_\mathrm{rUC}/2) \\ u_\mathrm{y}(x,y,\bar{t}_\mathrm{rUC}/2) \\ u_\mathrm{z}(x,y,\bar{t}_\mathrm{rUC}/2) \end{bmatrix} = \begin{bmatrix} 0 \\ 0 \\ \langle \varepsilon_z \rangle \, \bar{t}_\mathrm{rUC} \end{bmatrix}$$

$$\text{B6}\quad \begin{bmatrix} u_\mathrm{x}(-x,-y,\bar{t}_\mathrm{rUC}/2) \\ u_\mathrm{y}(-x,-y,\bar{t}_\mathrm{rUC}/2) \\ u_\mathrm{z}(-x,-y,\bar{t}_\mathrm{rUC}/2) \end{bmatrix} + \begin{bmatrix} u_\mathrm{x}(x,y,-\bar{t}_\mathrm{rUC}/2) \\ u_\mathrm{y}(x,y,-\bar{t}_\mathrm{rUC}/2) \\ -u_\mathrm{z}(x,y,-\bar{t}_\mathrm{rUC}/2) \end{bmatrix} = \begin{bmatrix} 0 \\ 0 \\ \langle \varepsilon_z \rangle \, \bar{t}_\mathrm{rUC} \end{bmatrix}$$

Nesting case 2: top ply: flipped, inverted, shifted; bottom ply: flipped, shifted

$$\text{B5I}\quad \begin{bmatrix} u_\mathrm{x}(-x+h_\mathrm{rUC}/2,-y,\bar{t}_\mathrm{rUC}/2) \\ u_\mathrm{y}(-x+h_\mathrm{rUC}/2,-y,\bar{t}_\mathrm{rUC}/2) \\ u_\mathrm{z}(-x+h_\mathrm{rUC}/2,-y,\bar{t}_\mathrm{rUC}/2) \end{bmatrix} + \begin{bmatrix} u_\mathrm{x}(x,y,\bar{t}_\mathrm{rUC}/2) \\ u_\mathrm{y}(x,y,\bar{t}_\mathrm{rUC}/2) \\ u_\mathrm{z}(x,y,\bar{t}_\mathrm{rUC}/2) \end{bmatrix} = \begin{bmatrix} \langle \varepsilon_x \rangle \, h_\mathrm{rUC}/2 \\ \langle \varepsilon_{xy} \rangle \, h_\mathrm{rUC}/2 \\ \langle \varepsilon_z \rangle \, \bar{t}_\mathrm{rUC} \end{bmatrix}$$

$$\text{B5II}\quad \begin{bmatrix} u_\mathrm{x}(-x-h_\mathrm{rUC}/2,-y,\bar{t}_\mathrm{rUC}/2) \\ u_\mathrm{y}(-x-h_\mathrm{rUC}/2,-y,\bar{t}_\mathrm{rUC}/2) \\ u_\mathrm{z}(-x-h_\mathrm{rUC}/2,-y,\bar{t}_\mathrm{rUC}/2) \end{bmatrix} + \begin{bmatrix} u_\mathrm{x}(x,y,\bar{t}_\mathrm{rUC}/2) \\ u_\mathrm{y}(x,y,\bar{t}_\mathrm{rUC}/2) \\ u_\mathrm{z}(x,y,\bar{t}_\mathrm{rUC}/2) \end{bmatrix} = \begin{bmatrix} -\langle \varepsilon_x \rangle \, h_\mathrm{rUC}/2 \\ -\langle \varepsilon_{xy} \rangle \, h_\mathrm{rUC}/2 \\ \langle \varepsilon_z \rangle \, \bar{t}_\mathrm{rUC} \end{bmatrix}$$

$$\text{B6I}\quad \begin{bmatrix} u_\mathrm{x}(-x-h_\mathrm{rUC}/2,-y,\bar{t}_\mathrm{rUC}/2) \\ u_\mathrm{y}(-x-h_\mathrm{rUC}/2,-y,\bar{t}_\mathrm{rUC}/2) \\ u_\mathrm{z}(-x-h_\mathrm{rUC}/2,-y,\bar{t}_\mathrm{rUC}/2) \end{bmatrix} + \begin{bmatrix} u_\mathrm{x}(x,y,-\bar{t}_\mathrm{rUC}/2) \\ u_\mathrm{y}(x,y,-\bar{t}_\mathrm{rUC}/2) \\ -u_\mathrm{z}(x,y,-\bar{t}_\mathrm{rUC}/2) \end{bmatrix} = \begin{bmatrix} -\langle \varepsilon_x \rangle \, h_\mathrm{rUC}/2 \\ -\langle \varepsilon_{xy} \rangle \, h_\mathrm{rUC}/2 \\ \langle \varepsilon_z \rangle \, \bar{t}_\mathrm{rUC} \end{bmatrix}$$

$$\text{B6II}\quad \begin{bmatrix} u_\mathrm{x}(-x+h_\mathrm{rUC}/2,-y,\bar{t}_\mathrm{rUC}/2) \\ u_\mathrm{y}(-x+h_\mathrm{rUC}/2,-y,\bar{t}_\mathrm{rUC}/2) \\ u_\mathrm{z}(-x+h_\mathrm{rUC}/2,-y,\bar{t}_\mathrm{rUC}/2) \end{bmatrix} + \begin{bmatrix} u_\mathrm{x}(x,y,-\bar{t}_\mathrm{rUC}/2) \\ u_\mathrm{y}(x,y,-\bar{t}_\mathrm{rUC}/2) \\ -u_\mathrm{z}(x,y,-\bar{t}_\mathrm{rUC}/2) \end{bmatrix} = \begin{bmatrix} \langle \varepsilon_x \rangle \, h_\mathrm{rUC}/2 \\ \langle \varepsilon_{xy} \rangle \, h_\mathrm{rUC}/2 \\ \langle \varepsilon_z \rangle \, \bar{t}_\mathrm{rUC} \end{bmatrix}$$

2.5. Generation of matrix pocket mesh for mechanical simulation

Now that the geometry of the yarns is defined in its final state, the addition of a matrix pocket mesh enables us to perform mechanical simulations of the composite unit cell. Particularly due to the non-orthogonal bundle interlacement and for highly compacted braids with their inherent complexity of the matrix pocket geometry, this step remains a major challenge in meso-FE modelling. Our approach relies on two basic principles: Firstly, an exact CAD representation of the matrix pocket geometry which serves as a surrogate for a periodic tetrahedral mesh is constructed through a series of boolean operations. Secondly, a search algorithm detects regions of mutual bundle contact and subsequently establishes interfacial cohesive zones. As a result, the meshing methodology allows us to create a coherent three-dimensional cohesive interface with local branching. There is no need for introducing am artificial matrix layer in between yarns, and poor tetrahedral element quality is avoided.

The overall procedure is explained in detail in Fig. 11. Initially, the deformed yarn mesh is tessellated in close proximity of the rUC with respect to its symmetries at the periodic boundaries, such that an assembly of multiple unit cells is constructed. Using spline interpolation in axial and transverse direction, a solid CAD representation of the textile is reconstructed based on the deformed nodal coordinates over multiple rUCs, as is shown in Fig. 11 (a) for a [0/±60] configuration. Owing to the actual mesh discretisation and small interpenetrations due to the previous penalty contact formulation, a direct boolean operation between two contacting yarns is not adequate. Independent of their mesh size, such a procedure would generate an ill-conditioned geometry features, including voids, self-intersecting surfaces or

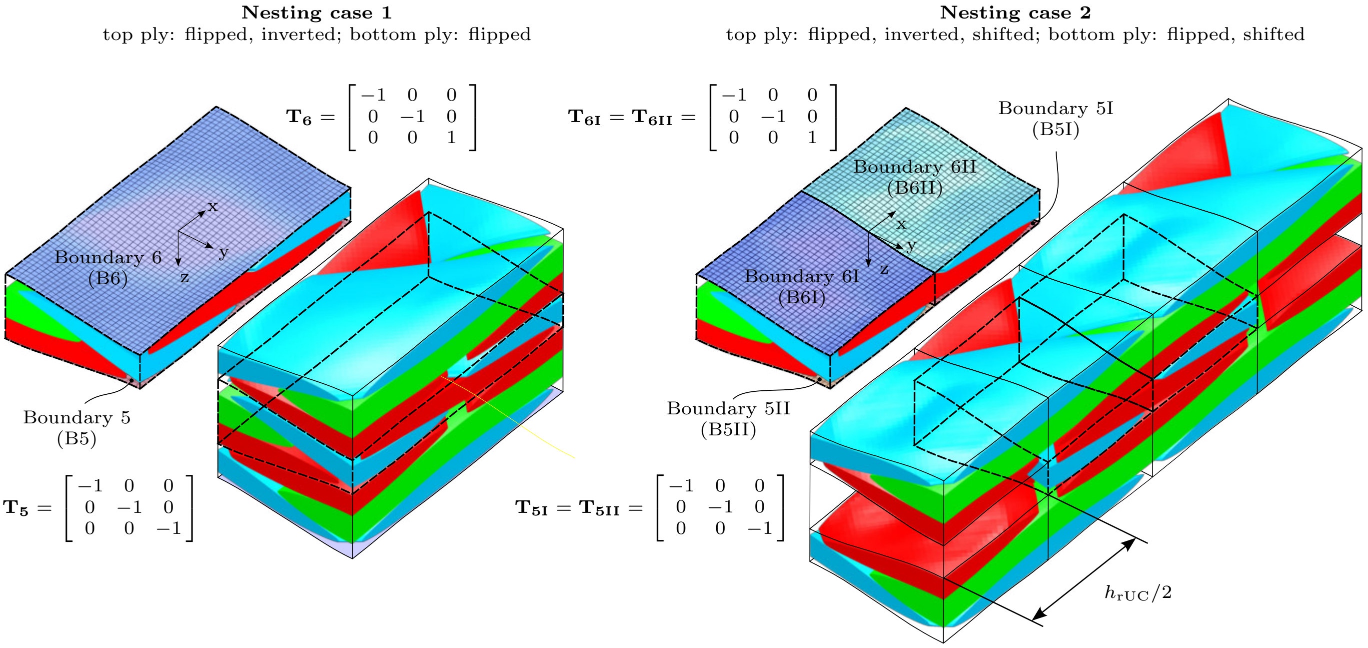

Nesting case 1
top ply: flipped, inverted; bottom ply: flipped

Nesting case 2
top ply: flipped, inverted, shifted; bottom ply: flipped, shifted

Figure 8: Out-of-plane PBCs considering nesting cases in unshifted and shifted configuration

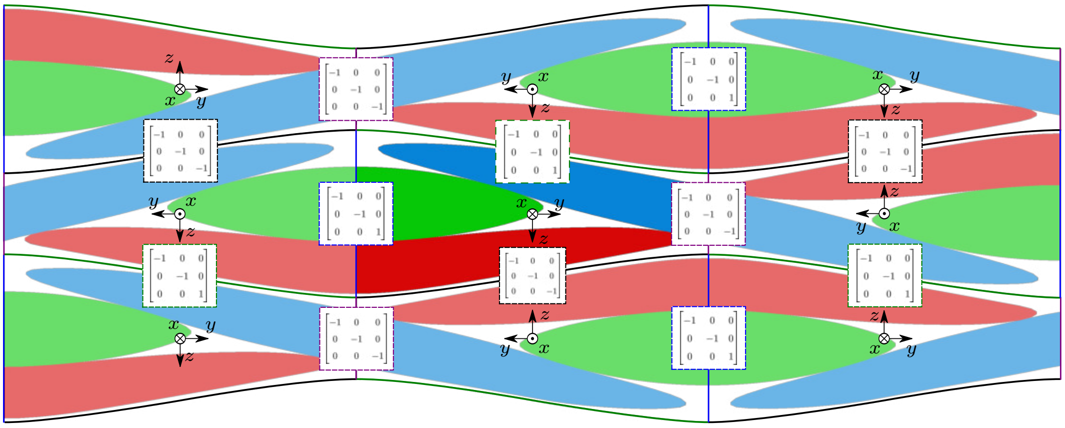

Figure 9: Interdependency of in-plane and out-of-plane PBCs for nesting case 1 satisfying periodic compatibility

very sharp angles that are impractical to mesh [8]. With the definition of a critical contact cut-off thickness t_{crit}, the presented algorithm automatically detects three-dimensional contact surfaces for every possible yarn interaction by performing geometric boolean operations on slightly thickened dummy bundles. For the envelopes of the resulting contact domains shown in Fig. 12, the distance between the CAD representation of two adjacent bundles is equal to the predefined cut-off thickness. If we move progressively to the centre of the contact area, the proximity decreases until both bodies locally interpenetrate each other. In case the geometric proximity between two potential contact partners exceeds the specified distance, the boolean operation yields a body of zero volume, indicating that no direct yarn-to-yarn contact is required. Now that the boundaries are defined, their automatic extraction is followed by the construction of the contact bodies as shown in Fig. 11 (b). Since this process extends over neighbouring unit cells, the assembled contact surfaces intrude into the simulation domain in such a way that all periodicity requirements are automatically satisfied at the boundaries. Now, the determination of the matrix pocket geometry is straightforward. At first, the contact bodies are removed from the rUC volume enclosed by the flexible membranes, then the yarns

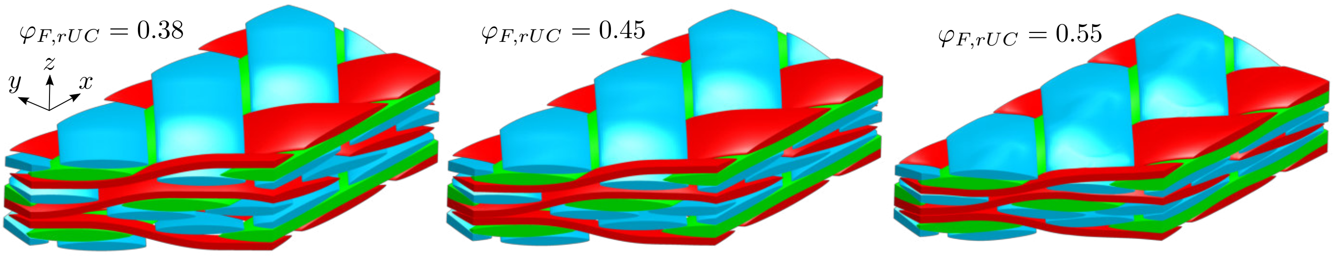

Figure 10: Evolution of global fibre volume fraction $\varphi_{\mathrm{F,rUC}}$ during compaction simulation for nesting case 1

are subtracted from the remainder to obtain the final CAD geometry highlighted in Fig. 11 (c). With the critical contact regions eliminated, the default meshing algorithm is now capable of generating a high quality solid tetrahedral mesh. To satisfy the periodicity requirements, a two-dimensional mesh is initially created at predefined seed faces at the boundaries. By applying the coordinate transformation matrices, this source mesh seed is transformed into its corresponding target morphology and then copied accordingly. The top and bottom surfaces of the completed mesh highlighted in Fig. 11 (d) are assembled from the deformed nodal coordinates of the flexible membranes which retain their periodicity during the compaction process.

For the purpose of modelling delamination between the yarns and the bulk resin, a layer of three-dimensional cohesive elements is extruded on top of the tetrahedral matrix mesh, much like an interior coating. This thin layer shares coincident nodes with the tetrahedral matrix elements on one side. Subsequently, the direct yarn-to-yarn cohesive interface zones are added to the global mesh. After cropping their geometries to the rUC boundaries, these regions are discretised with cohesive elements separately. However, due to consistent mesh seed sizes, the coordinates of nodes created at the outer circumference of each yarn-to-yarn contact domain match those of the adjacent yarn-to-matrix cohesive zone. Along this transition line shown in Fig. 11 (f), a single yarn-to-yarn cohesive interface branches into two diverging yarn-to-matrix interfaces with underlying tetrahedral elements. Here, both cohesive zones are connected by merging the outer yarn-to-yarn interface nodes with the respective upper and lower partner nodes of adjacent yarn-to-matrix cohesive elements, such that a seamless connection is achieved. The resulting smooth interfacial transition enables us to capture propagation and branching of cohesive cracks. While the cohesive elements share nodes with the underlying tetrahedral mesh on their inner side, their outer surfaces displayed in Fig. 11 (e) must be coupled to the yarns in order to ensure displacement continuity across the interface. Due the inherent geometrical incompatibility of hexahedral and tetrahedral element types and the absence of pyramidal elements in Abaqus (6.14) [26], the mesh coupling is achieved by means of a tie formulation. As opposed to the approach described in [22], however, no artificial matrix layer between the yarns is necessary, and the periodic nature of the matrix mesh eliminates any need for an additional interpolation at the boundaries. For the tie implementation, the solver specific surface-to-surface formulation guarantees a smooth and accurate stress distribution at all interfaces by enforcing constraints in an integral sense over a finite region, rather than at discrete nodes as in the traditional node-to-surface approach [26]. The inner nodes of the cohesive elements are excluded from the PBC definition at the periodic boundaries. Otherwise, over-constraints would either issue an input error or lead to a significant increase in simulation run time, depending on whether the implicit or explicit solver is used. Here, periodicity of the nodal displacements is implicitly enforced through the master role of adjacent yarn nodes in the tie formulation.

The effect of the presented methodology on the interfacial stress distribution is shown in Fig. 13 for an axial yarn of the [0/±45] braid loaded in transverse direction. Owing to the stiffness discontinuity at the interface transition line, where a single cohesive element branches into a stack of tetrahedral matrix elements covered by a thin cohesive zone on both sides, these regions develop minor stress concentrations compared to their undisturbed surroundings. However, the overall distribution of the traction components is preserved well. Given the low intensity of the artificial stress concentrations at the interface junction, it can be concluded that the overall stress distribution in the interface is captured well by the meshing methodology. Similar to the yarn meshing procedure, this methodology may be easily adapted to a variety of textile composites, allowing for a more realistic representation of branching interfaces without the need of introducing a dummy matrix mesh of finite thickness in between contacting yarns. In addition, the proposed methodology offers several advantages:

- since the contact search algorithm reconstructs a CAD geometry based on spline interpolation of the deformed nodal coordinates, the resulting contact search is less sensitive to the mesh density due to the inherent geometrical smoothing effect
- no modifications or distortions of the yarn mesh are required
- by working on CAD geometry, error prone nodal search algorithms are avoided

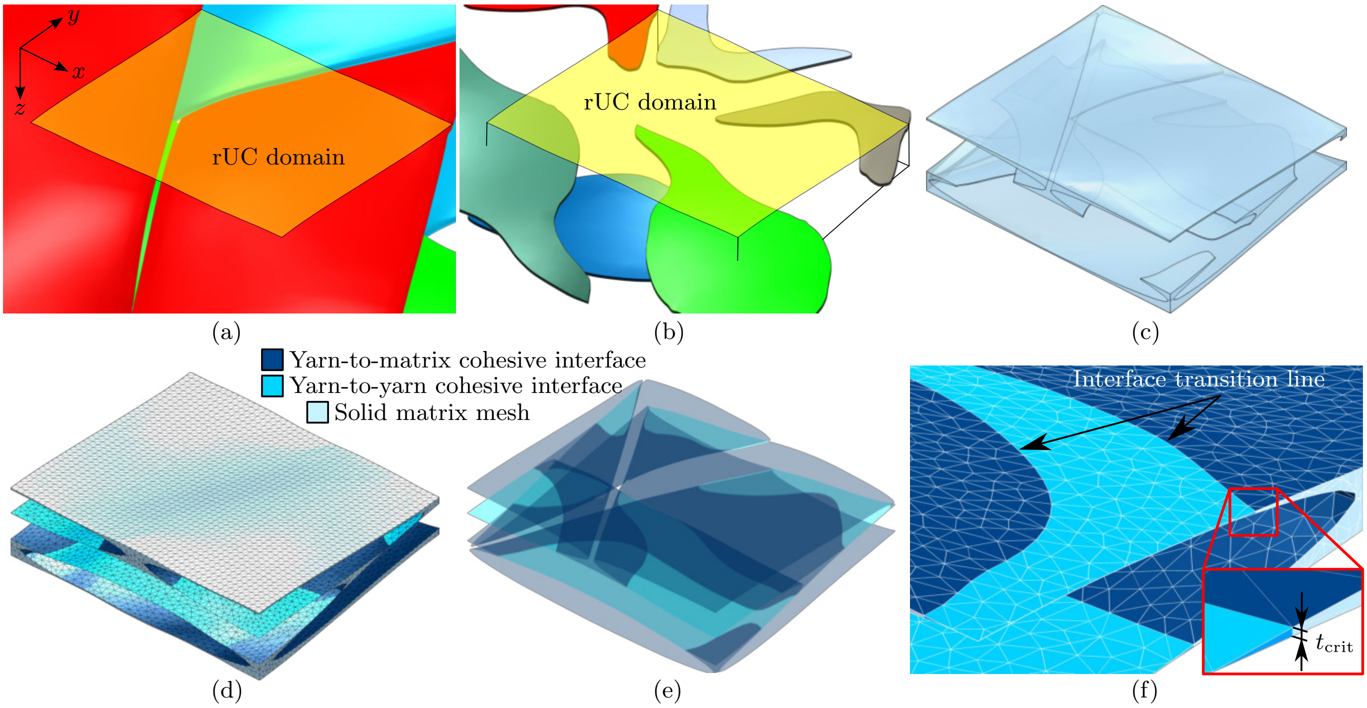

Figure 11: Algorithm for generation of matrix pockets mesh: (a) CAD reconstruction of compacted yarn mesh, (b) determination of direct yarn-to-yarn direct contact zones, (c) CAD model of matrix pockets, (d) final mesh of matrix pockets, (e) cohesive zones highlighted and (f) detailed view of a transition zone of the yarn-to-yarn and yarn-to-matrix cohesive mesh

3. Validation and application

With the simulation framework defined, we apply our methodology to predict the elastic properties of triaxial braided composites. The materials in this study are manufactured from Toho-Tenax HTS40 F13 12K (800 tex) untwisted yarns for both the axial and braid direction in combination with a Hexcel HexFlow RTM 6 epoxy resin. In order to

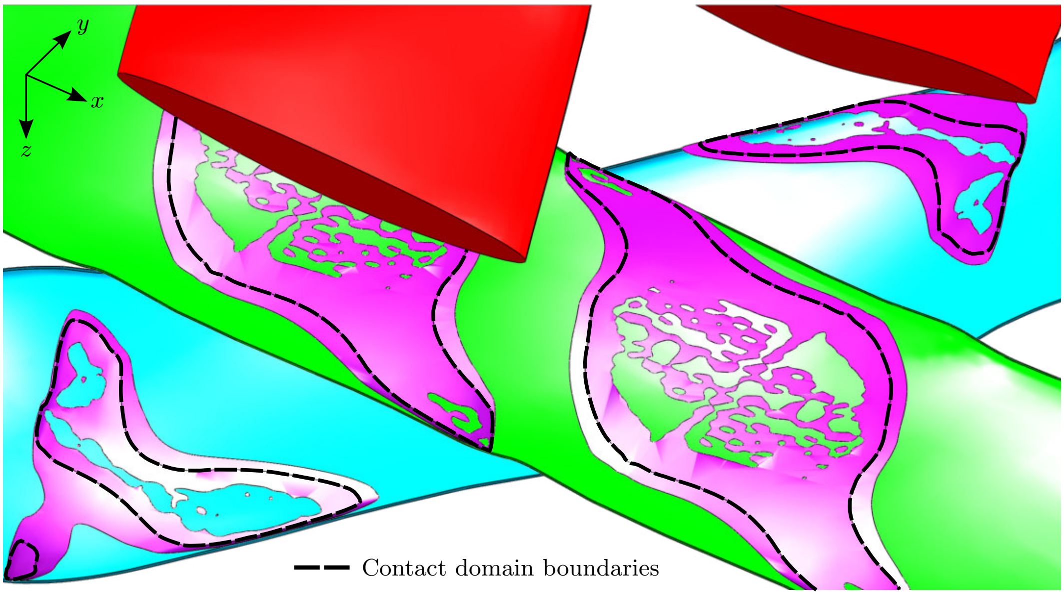

Figure 12: Determination of yarn-to-yarn contact regions and extraction of domain cut-off boundaries

demonstrate the framework, various unit cells are generated for braiding angles ranging from 25° to 65° in increments of 5°. For validation purposes, tensile tests of straight-sided specimens with a total of four layers are performed in accordance with ASTM D3039 [38]. Three braid architectures, with a nominal braiding angle of 30°, 45° and 60° are each tested in their longitudinal (x), transverse (y) and braid yarn direction ($1F$). Details on the manufacturing process and the elastic properties are summarised in [37].

Based on a mesh refinement study, an average element seed size of $70\,\mu$m is selected for all unit cells. Given the geometrical properties of the bundles under investigation, this discretisation yields approximately 40 hexahedral elements with incompatible modes over the yarn width and two elements in the thickness direction, with a total of 7036 elements for the [0/±30], 9120 for the [0/±45] and 9114 for the [0/±60] configuration. Depending on the braiding angle, roughly 15,000 and 20,000 cohesive elements ensure coupling with the matrix pockets that contain in between 40,000 to 50,000 tetrahedral elements. For all unit cells, a bundle side thickness ratio of $\xi_\mathrm{a} = \xi_\mathrm{b} = 5\%$ is selected.

3.1. Internal geometry

Ensuring that the unit cell models render a realistic representation of the compacted internal textile geometry is key for accurate predictions of the mechanical response. A detailed reconstruction of the actual geometry from μCT measurements enables us to identify key geometrical features and compare them to the model. These parameters comprise the yarn centre-line, thickness, width, spacing, twist, and the intra-yarn FVF calculated from the cross-sectional area for both the axial and braid fibre bundles. In addition, we can study the periodic nature of the internal geometry, evaluate its spatial variability and asses the applicability of a unit cell modelling approach to the problem. For each textile architecture, samples of $15 \times 15 \times 3\,\mathrm{mm}^3$ were cut from the resin-infused plates in close proximity to the coupons used for the mechanical tests and scanned with a GE Phoenix/X-Ray Nanotom 180 at a voxel size of $9\,\mu\mathrm{m}^3$ at the University of Applied Sciences Upper Austria. Since an automatic segmentation of resin-infused bundles poses significant challenges [39], a semi-automatic segmentation strategy was developed. Initially, the raw CT data is imported into a Matlab script and sliced using three planes, with each of them corresponding to a cut orthogonal to one of the in-plane fibre directions. Within the resulting stacks of CT images, solely the cross-sections normal to

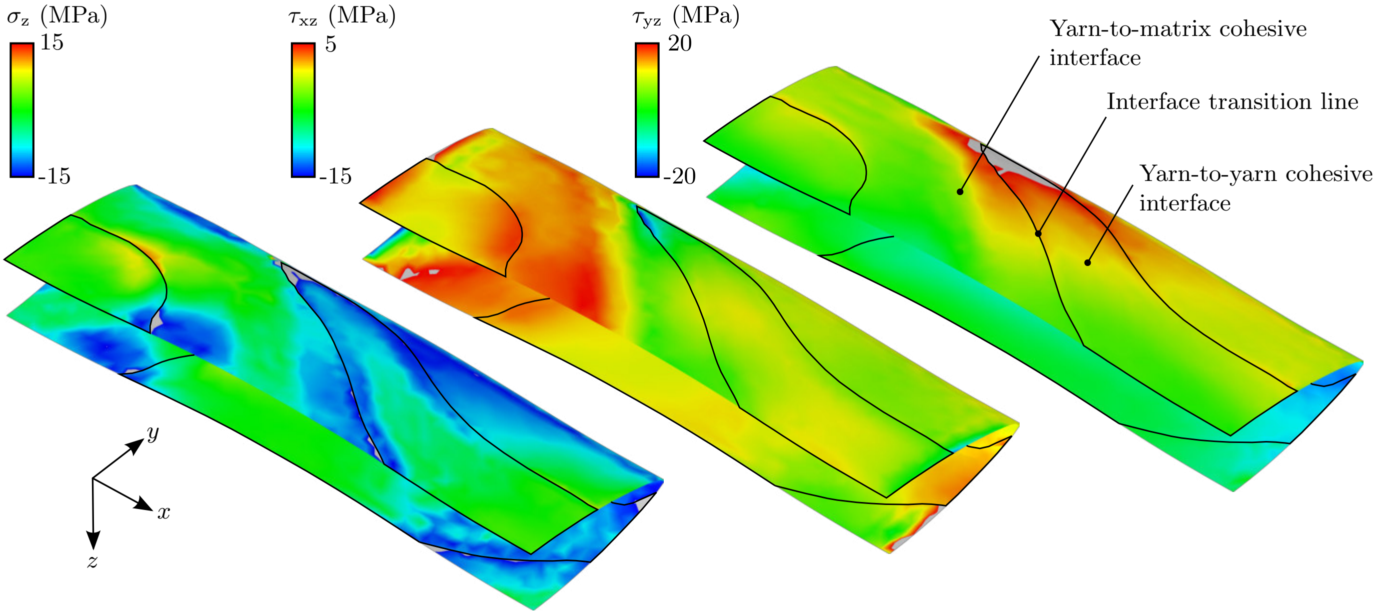

Figure 13: Effect of the proposed yarn-to-yarn and yarn-to-matrix cohesive meshing methodology on the interfacial stress distribution of half of an axial yarn of a [0/±45] braid loaded in transverse direction

the cut plane are segmented manually by a predefined number of points that form a closed polygon line at the bundle perimeter. This procedure is repeated until all cross-sections along each image stack are processed. To minimise the manual input during this cumbersome procedure, existing points are automatically copied to subsequent images where only minor adjustments are required. As the data is progressively visualised and saved, changes to any of the cross-sections can be made at any time via a graphical user interface. A minimum of statistical data is captured along each yarn path by limiting the segmentation to entities that extend at least over a single undulation interval inside the measurement volume. In the presented study, each cross-section is manually discretised with 20 measurement points. The distance between two consecutive cross-sections is 180 μm for the braid and 540 μm for the axial direction. In total, the segmentation of the [0/±30] material involves 37900 points, the [0/±45] 43100 points and the [0/±60] braid 40460 points. Finally, the data set is converted into a 3D CAD geometry using spline interpolation in both axial and transverse direction for easy inspection of geometrical features and comparison with the unit cell models. For the generation of the unit cell models at arbitrary braiding angles, we apply a quadratic interpolation function on the basis of the averaged μCT geometry that is summarised in Table 3. The global FVF measurements $\varphi_{\mathrm{F,rUC}}$ were obtained using acid digestion in accordance with ASTM D3171 [40].

Table 3: Averaged μCT geometry used for the generation of the unit cell models

Global		Axial yarns						Braid yarns					
θ	$\varphi_{\mathrm{F,rUC}}$	s_{a}	w_{a}	t_{a}	κ_{a}	A_{a}	n_{a}	s_{b}	w_{b}	t_{b}	κ_{b}	A_{b}	n_{b}
(deg)	(%)	(μm)	(μm)	(μm)	(%)	(mm^2)		(μm)	(μm)	(μm)	(%)	(mm^2)	
30	56 ± 0.9	3354 ± 123	2122 ± 131	452 ± 90	66 ± 6	0.674 ± 0.029	0.76	3052 ± 583	2695 ± 267	326 ± 59	70 ± 5	0.660 ± 0.048	0.58
45	55 ± 0.8	4232 ± 118	2340 ± 157	440 ± 43	66 ± 4	0.726 ± 0.041	0.74	3047 ± 288	2716 ± 187	327 ± 50	70 ± 6	0.661 ± 0.054	0.60
60	56 ± 0.2	6003 ± 259	2888 ± 203	350 ± 45	63 ± 5	0.742 ± 0.059	0.63	2799 ± 233	2767 ± 175	317 ± 59	70 ± 5	0.663 ± 0.060	0.56

The centre-lines shown in Fig. 14 for the [0/±45] braid are extracted from the geometrical area centroid of consecutive cross-sections along the axial and braid fibre undulation path. After segmentation, the individual curves are superimposed and averaged locally to allow a comparison with the compacted unit cell geometry. For the braid yarns displayed in Fig. 14 (a), the periodic nature of the fibre waviness is clearly evident. When following individual bundle loci, we encounter greater deviations from the experimental average, particularly in close proximity to regions of peak amplitude. Here, the nesting configuration during compaction plays a key role in the formation of the overall internal geometry. When braid bundles of equal orientation are positioned on top of each other, the mutual interaction can flatten their undulation path over a finite contact length. During compaction and subsequent resin infusion, they merge into a bundle devoid of a visible interface in this region. If we analyse each of the centre-lines separately, we observe a certain degree of geometric variability induced by manufacturing process chain, much like superimposed high frequency noise. However, as soon as a critical number of yarn loci is combined in a statistical analysis, the average path follows a clear periodic trend with a comparable standard deviation bandwidth. If the first nesting case is considered in the simulations, the average experimental shape is captured very well. Here, the positioning of the braid yarns in the thickness direction promotes nesting into cavities that form in regions where the bundles progressively thin out along their width. Due to the lack of a supporting yarn at about half of the distance between the point of maximum and zero undulation amplitude, the braid yarns are compacted inwards and the yarn path exhibits a slight kink. In the second nesting case, the centre-lines of the braid yarns are arranged directly on top of each other. Using coincident geometric input parameters, they develop an undulation plateau with a slightly smaller amplitude at the intersection with an axial bundle. At this point, the yarn are tightly packed. Hence, large compaction stresses translate into yarn flattening and hence a higher degree of geometrical defects in the textile architecture.

The experimental findings in Fig. 14 (b) confirm the existence of additional fibre waviness in the axial bundles, although at a significantly reduced amplitude compared to the bias direction. The individual experimental curves are shifted to achieve an optimum correlation in their first positive undulation interval. Here, the average undulation path and the simulations with both nesting cases match extremely well in terms of wavelength and amplitude. As we progressively move away from the correlation point, fundamental changes in the shape of the centre-lines are accompanied by a sky-rocketing standard deviation. These findings indicate that the degree of fibre waviness in the axial yarns is driven by local bending effects dominated by the nesting configuration. The simulated nesting cases were found to have only minor impact on the yarn path of the unit cell. During the compaction, the initially straight axial bundles are subjected to local bending from their entangling braid counterparts, independent of the applied out-of-plane boundary conditions. While we cannot identify a clear periodic trend of axial fibre waviness in the experiments, the unit cell model captures this geometrical phenomenon in terms of amplitude and wavelength and hence also renders possible effects on the mechanical response.

In addition to the centre-lines, the textile architecture is characterised by a variety of geometrical parameters. As exemplarily displayed in Fig. 15 for the braid bundles of the [0/±45] configuration, the yarn width w_{b}, thickness t_{b}, intra-yarn FVF κ_{b} and twist angle α_{b} are analysed along the average experimental undulation path. Assuming an undamaged 12k bundle and a fibre diameter of $7\,\mu m$, the intra-yarn FVF is obtained for each cross-section by relating the total filament area to the total segmented area. Each cross-section and the corresponding yarn thickness are calculated orthogonal to the local yarn path direction.

When we investigate the evolution of the average braid yarn width w_{b} along its undulation path z'_{b} in Fig. 15 (a), we discover a periodic increase each time it converges to its peak amplitude. Looking at the distribution of the average thickness t_{b} in Fig. 15 (b) at the same time, an opposite trend is clearly visible. This change in aspect ratio is further accompanied by a repeating growth of the intra-yarn FVF in Fig. 15 (c) at coincident positions along the undulation path. These finding underline the impact of the compaction process on the bundle geometry. In regions where yarns of

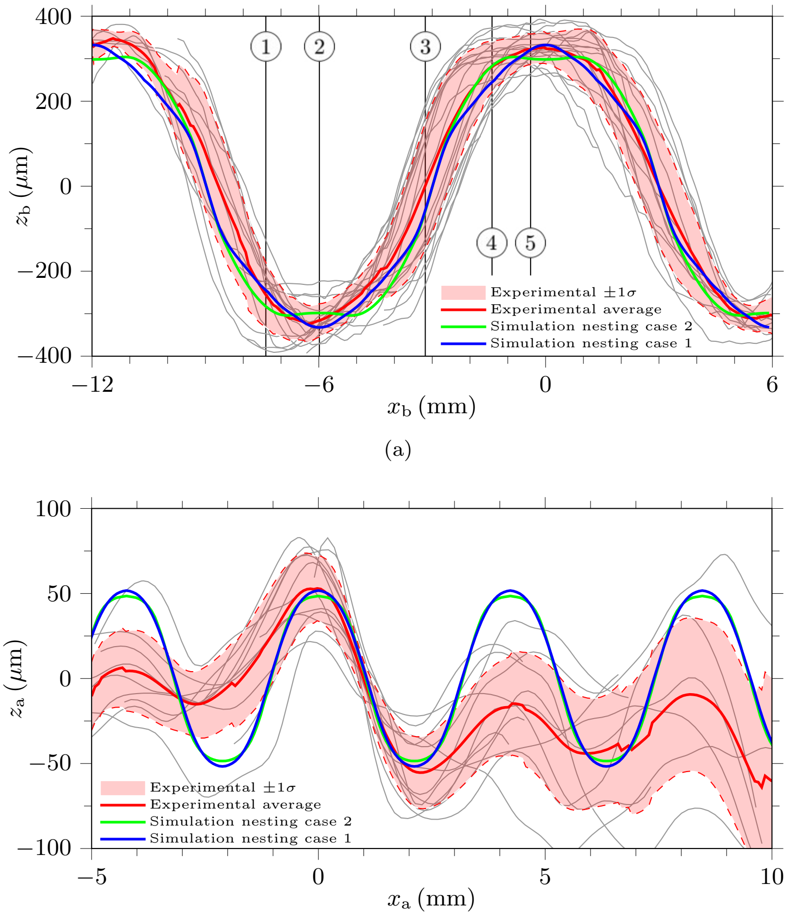

(a)

(b)

Figure 14: Comparison of experimental and simulated yarn path of the [0/±45] braid for (a) braid yarns (b) axial yarns (see Fig. 16 for braid yarn cross-sections at positions ① to ⑤)

adjacent plies are in direct contact, their cross-sections are flattened under the applied pressure. In these regions where the elevated intra-yarn FVF levels are consistent with a tight fibre packing, dry contacting filaments are subjected to a transverse movement and the bundles are subsequently widened. Recalling that the primary focus of the simulation framework is to construct a defect enriched geometry model based on average geometrical parameters of the finished composite, only minor variations of the geometrical parameters are rendered in the unit cell. While the bundle width is largely unaffected by the compaction simulation and its stacking configuration, the second nesting case produces a slight variation in the thickness and intra-yarn FVF distribution. Again, with bias bundles of adjacent plies positioned directly on top of each other, a flattening mechanism similar to the one found in the μCT experiments is introduced. The distortion of fibre bundles along their undulation path is hard to quantify, especially since the cross-sections typically do not exhibit uniform twisting. For a more detailed comparison of the experimental and the simulated topology, we introduce a twist angle α derived from the orientation of the principal axes of the second area moment tensor defined as:

$$\alpha = \frac{1}{2}\arctan\left(\frac{2\,I_{\mathrm{y'z'}}}{I_{\mathrm{y'}} - I_{\mathrm{z'}}}\right), \tag{9}$$

where the tensor components $I_{\mathrm{y'}}$, $I_{\mathrm{z'}}$ and $I_{\mathrm{y'z'}}$ with respect to the yarn cross-sectional area centroid are obtained from numerical integration and the sign of α follows a right-handed coordinate system. When looking at the distortion of positively oriented braid yarns in Fig. 15 (d), we notice a periodic response characteristic of their waviness. At the point of maximum path amplitude, they are located directly on top of their axial counterparts. During the transition into the downwards undulation segment, the mutual contact induces a gradual distortion in the braid bundles as they are forced to accommodate to the underlying cross-section. This phenomenon is consistent with the first sinusoidal peak of the twist angle α_{b}. At the point of maximum out-of-plane curvature, the fibres further pass through the gap of two neighbouring longitudinal bundles. Owing to the absence of an interacting axial bundle at this point, the overall distortion is minimised. Although the bundle now continues on the opposite side of the textile, a second peak is created by the identical kinematics near the successive intertwining region. Further along the centre-line, the mechanism is continuously repeated, with the exception that the orientation of the twist angle changes sign in the upwards path segment. The unit cell model captures this phenomenon accurately. Consistent with the higher overall distortion, the second nesting predicts a sharper shape of the twist angle distribution.

A detailed comparison of the experimental and the simulated yarn cross-sections in both braid directions is shown in Fig. 16 at different locations along the centre-lines indicated in Fig. 14 (a). Superposition of the cross-sections is achieved by shifting each area centroid to the origin of the local coordinate system. The first virtual cut ① is made halfway between the point of maximum and zero undulation amplitude, where the simulated yarn shapes experience the largest degree of twisting. While the magnitude and the opposing twist directions in the positive and negative braid bundles agree well with the μCT measurements, we observe considerable scatter in the latter, further indicating that their deformation during compaction is sensitive to the local nesting configuration. Moving further along the centre-line, the second cut ② investigates the point of maximum undulation amplitude. Here, the braid yarns are pressed against their axial counterparts as a result of direct contact with bundles from neighbouring layers. While the unshifted stacking configuration in nesting case 2 produces a flattened top and bottom surface, additional bending is introduced across the yarn width as a result of the shifted locations of braid bundles through-the-thickness in nesting case 1. The resultant asymmetric shape correlates well with the characteristic deformation mode of the actual cross-sections at this location, similar to the mechanism found in woven composites [18]. Contrarily to the previous cases, we observe mostly undistorted yarn-shapes and a low scatter near the point of zero undulation amplitude ③, where the fibres exhibit their maximum crimp angle. As a bundle crosses from one side of the textile to the other, the degree of interaction with adjacent plies and subsequent deformation are minimised. Position ④ coincides with the first cut in the upwards undulation segment and repeats the characteristic deformation pattern, although the sign of twist deformation changes. In the final cross-section ⑤ slightly before the peak amplitude, the gradual development of the yarn flattening mechanism is again encountered in opposite direction.

In Fig. 17, the evolution of the average ply thickness $\bar{t}_{\mathrm{rUC,c}}$ is outlined as a function of the global FVF $\varphi_{\mathrm{F,rUC}}$. At the beginning of the compaction simulation, all three braid architectures comprise a global FVF of approximately 37%. During their initial interaction, the bundles reposition freely and fill up large voids while the overall thickness drops considerately.

Close to the target FVF, the mutual contacts multiply. Due to the inherent growth in compaction resistance, the slope of the thickness reduction declines consistently. In comparison to the experimental data obtained from calliper measurements of the plate thickness, the simulated target values agree well. To validate the quasi-incompressible material behaviour during the compaction simulation, the total change in yarn volume is investigated in Fig. 18. For configurations involving the first nesting case, a negligible volumetric change is encountered. More pronounced but

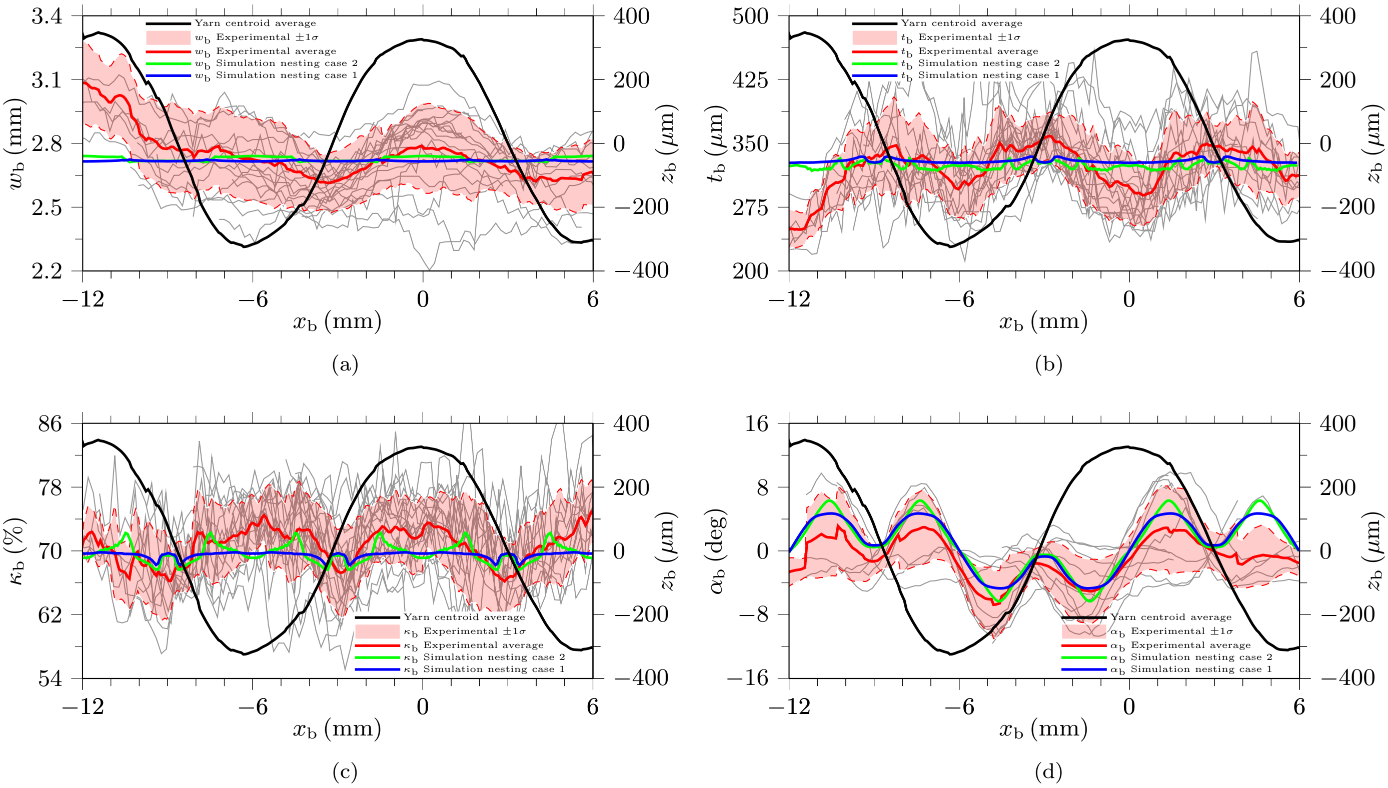

(a) (b) (c) (d)

Figure 15: Comparison of experimental and simulated yarn architecture of the [0/±45] braid (a) bundle width w_b (b) bundle thickness t_b (c) intra-yarn FVF κ_b, (d) twist angle α_b

still in an acceptable range, the second nesting case induces a total volumetric shrinkage of approximately 0.5%. Here, the direct contact of two overlapping braid bundles from adjacent plies produces excessive contact pressure and local distortion.

In order to assess the sensitivity of the compacted geometry and the resulting stress fields with respect to the mesh density, a mesh refinement study was performed. A total of four unit cells of the same [0/±45] architecture in the first nesting configuration were created with the properties of each mesh highlighted in Table 4. In addition to varying the input element seed size l_mesh from its nominal value of $70\,\mu$m (medium) to $45\,\mu$m (fine) and $105\,\mu$m (coarse), the number of elements in the yarn through-thickness direction was doubled for the nominal case. As the meshing algorithm in the resin pockets adjusts for this modification at the truncated yarn sides, both medium mesh topologies feature a slightly different discretisation of the matrix pockets. For the side edges of the bundles, a thickness ratio of $\xi = 5\%$ was selected for all unit cells throughout this work.

The effect of the different mesh sizes on the compacted yarn path is investigated in Fig. 19 along a single undulation interval (a) at the top position and (b) at the side of the braid bundles. We quantify the relative positional error by comparing the nodal coordinates of each mesh with respect to the finest discretisation. Following the nodal coordinates at the top position of the bundle along a single undulation interval in Fig. 19 (a), we can identify two characteristic peaks in the geometrical error, with the larger one coinciding to the location of direct contact with an entangled axial bundle close to the minimum path locus. Although the identical phenomenon is again encountered at the top of the undulation path, its severity is dampened by larger distance to the output location. While the shape of the yarn path deviation is mostly independent of the mesh, the relative error reduces gradually as a function of the mesh refinement.

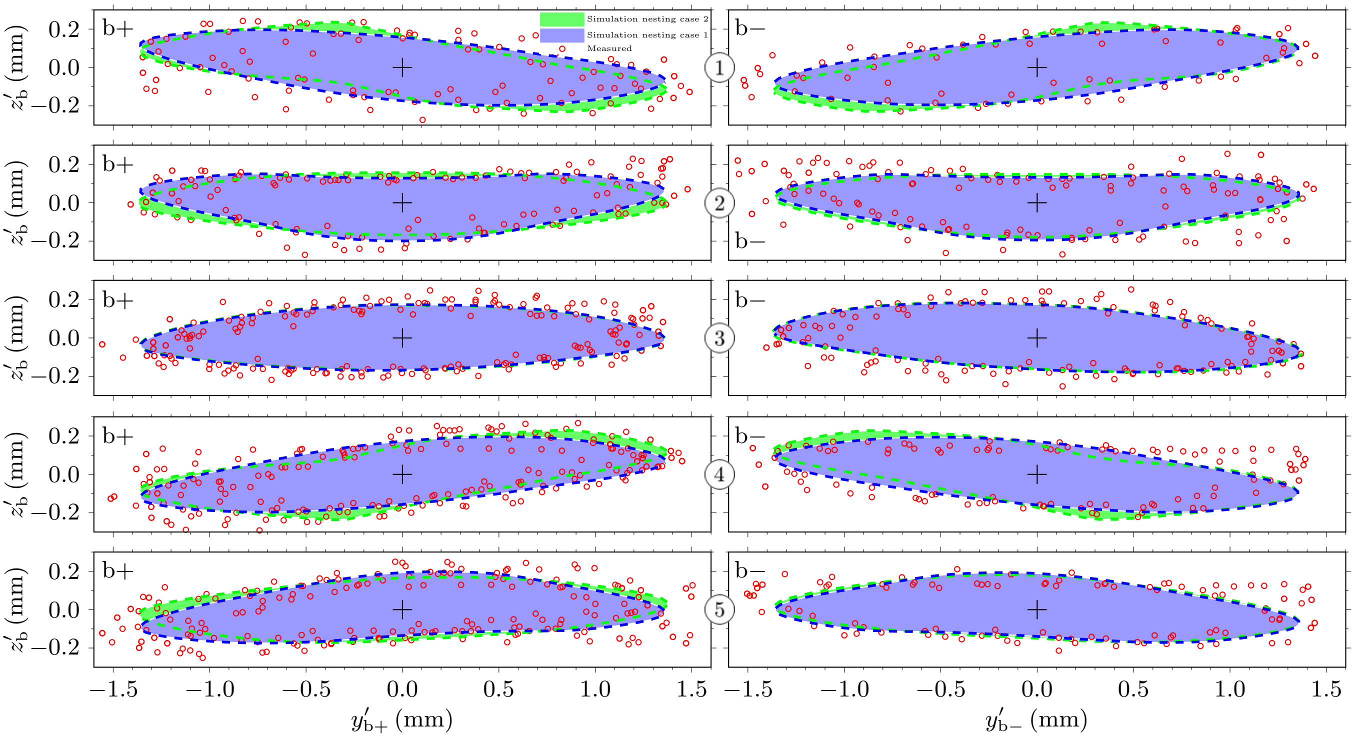

Figure 16: Comparison of experimental and simulated cross-sections for positively (b+) and negatively (b−) oriented braid yarns of the [0/±45] braid at position ① to ⑤

A significantly better convergence, however, is achieved by increasing the element count in the yarn thickness direction, as local deformations at the mutual contact zones can be captured more accurately. The same tendency can be found at the yarn side locus in Fig. 19 (b). While still having the highest error magnitude, the path predicted by the coarse mesh changes sign compared to all other configurations near the point of zero undulation amplitude, where axial and braid yarns interlock. Given the low overall sensitivity of the compacted geometry with respect to the mesh density, it can be concluded that the compacted textile architecture can be reliably reproduced with the given normal mesh size of $l_{\mathrm{mesh}} = 70\,\mu$m.

Table 4: Mesh statistics of the [0/±45] braid refinement study ($\xi_{\mathrm{a}} = \xi_{\mathrm{b}} = 5\%$)

Mesh density	Fine	Medium	Medium	Coarse
l_{mesh} (μm)	45	70	70	105
Elements per yarn thickness	4	4	2	2
Elements in yarns (hex)	39512	17328	8664	4064
Elements in yarns (wedge)	1392	912	456	312
Elements in matrix pockets (tet)	118187	41776	40787	17016
Elements (3D cohesive)	44295	16564	16234	8977
Elements total	203386	76580	66141	30369
Nodes in yarns	52410	23665	14199	6927
Nodes in matrix pockets	59339	22649	22175	11796
Nodes total	111749	46314	36374	18723

3.2. Elastic properties

After updating the local fibre orientations for the compacted yarns, elastic properties can be readily obtained through the application of principal load cases and subsequent homogenisation. The material properties of the linear elastic

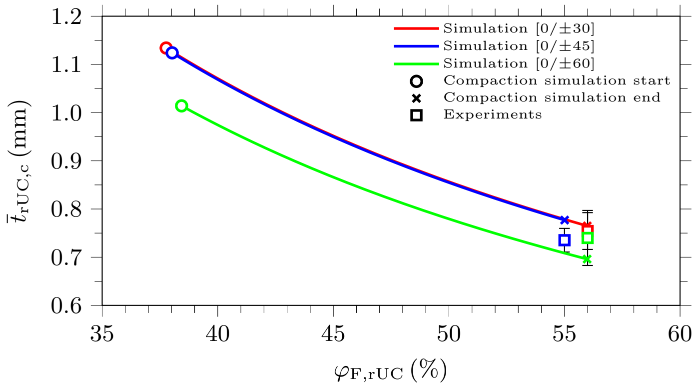

Figure 17: Evolution of average ply thickness $\bar{t}_{\mathrm{rUC,c}}$ as a function of the global FVF $\varphi_{\mathrm{F,rUC}}$ during the compaction simulation for nesting case 1

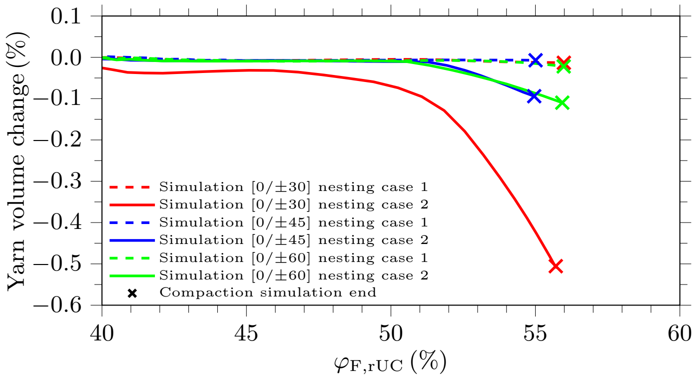

Figure 18: Total yarn volume change as a function of the global FVF $\varphi_{\mathrm{F,rUC}}$ during the compaction simulation

transversely isotropic bundles summarised in Table 5 are calculated from the fibre and matrix properties given in Table 6 using Chamis' micromechanical equations [41] at the intra-yarn FVFs κ from Table 3. For a rUC subjected to a sequence of four successive linear load cases (E_{x}, E_{y}, E_{z}, G_{xy}) combined in a single simulation, the model is solved by Abaqus/Implicit (6.14) within seconds on a standard computer.

Table 5: Elastic properties of the transversely isotropic yarns for characteristic intra-yarn FVFs

κ (%)	E_1 (MPa)	$E_2 = E_3$ (MPa)	$G_{12} = G_{13}$ (MPa)	$\nu_{12} = \nu_{13}$	ν_{23}
63	133369	8660	4364	0.322	0.388
66	139583	9087	4705	0.320	0.391
70	147867	9709	5236	0.319	0.395

The unit cell predictions are compared to an analytical model, where the out-of-plane waviness of the braid yarns is taken into account by averaging their local elasticity tensor $\mathbf{C}_{\mathrm{b}}(x_{\mathrm{b}})$ along the idealised yarn path discussed in Section 2.2 [42]. Assuming iso-strain conditions along half of the wavelength L_{u}, the homogenised elasticity tensor $\langle \mathbf{C}_{\mathrm{b}} \rangle$ for the braid bundles is calculated from

$$\langle \mathbf{C}_{\mathrm{b}} \rangle = \frac{1}{L_{\mathrm{u}}} \int_0^{L_{\mathrm{u}}} \mathbf{C}_{\mathrm{b}}(x_{\mathrm{b}}) \, \mathrm{d}x_{\mathrm{b}} \tag{10}$$

For triaxial braided composites, the macroscopic elastic properties are obtained by constructing an equivalent laminate

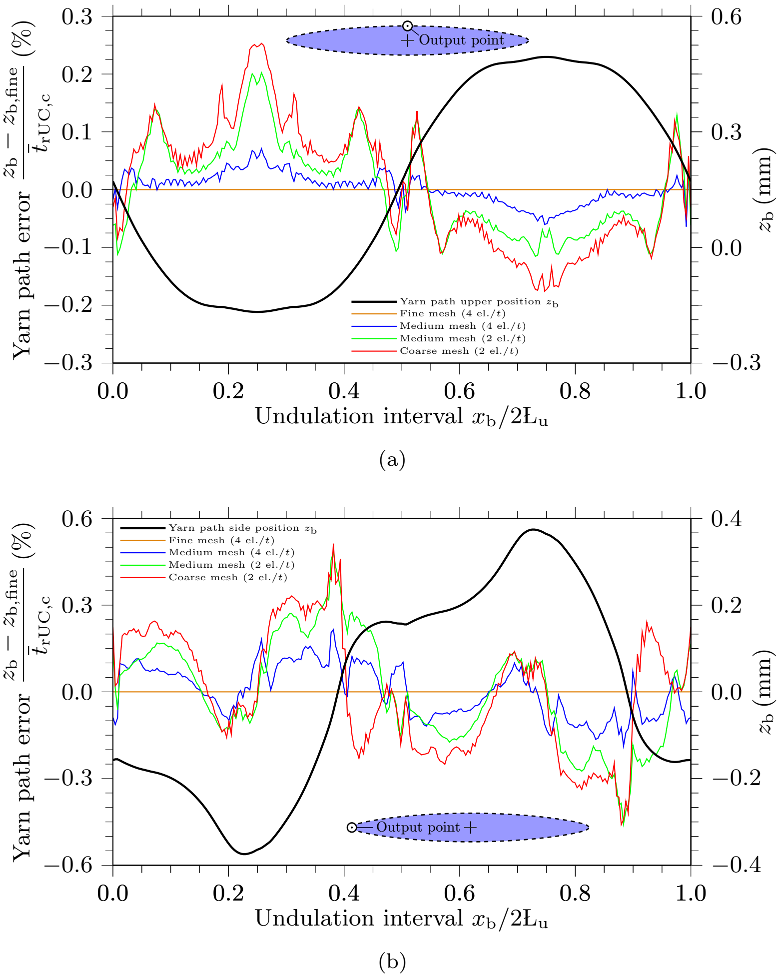

(a)

(b)

Figure 19: Relative yarn path error along a single undulation interval (a) at the top position and (b) at the side of the braid bundles

using classical lamination theory (CLT). The axial yarns, the braid yarns and the pure resin pockets are virtually separated and each of the constituents is then modelled either with a single unidirectional ply in the respective fibre direction or represented by an isotropic layer, as is the case for the matrix pockets. The relative ply thicknesses t_a/t and t_b/t in the laminate model correspond to the volume fractions of axial and braid yarn content V_a/V and V_b/V

Table 6: Elastic properties for fibre and resin [36]

Fibre: Toho-Tenax HTS40 F13 (12K, $\mu_{\text{F,yarn}} = 800\,\text{tex}$)						Resin: RTM 6	
$E_{1\text{f}}$ (MPa)	$E_{2\text{f}}$ (MPa)	$G_{12\text{f}}$ (MPa)	$\nu_{12\text{f}}$	$\nu_{23\text{f}}$	ρ_{F} (g/cm^3)	E_{m} (MPa)	ν_{m}
210000	18000	21800	0.305	0.450	1.76	2890	0.35

and vary as a function of the braiding angle θ and the yarn properties. From a 2D unit cell, they are related by:

$$\begin{aligned}
\frac{V_\mathrm{a}}{V} &= \frac{t_\mathrm{a}}{t} = \frac{\varphi_\mathrm{F}}{\kappa_\mathrm{a}\left(1+\dfrac{2}{\cos(\theta)}\,\dfrac{\rho_\mathrm{F,a}\,\mu_\mathrm{F,yarn,b}}{\rho_\mathrm{F,b}\,\mu_\mathrm{F,yarn,a}}\right)}\\
\frac{V_\mathrm{b}}{V} &= \frac{t_\mathrm{b}}{t} = \frac{\varphi_\mathrm{F}}{\kappa_\mathrm{b}\left(1+\dfrac{2}{\cos(\theta)}\,\dfrac{\rho_\mathrm{F,a}\,\mu_\mathrm{F,yarn,b}}{\rho_\mathrm{F,b}\,\mu_\mathrm{F,yarn,a}}\right)}\\
\frac{V_\mathrm{m}}{V} &= \frac{t_\mathrm{m}}{t} = 1-\frac{V_\mathrm{a}+V_\mathrm{b}}{V} = 1-\frac{t_\mathrm{a}+t_\mathrm{b}}{t},
\end{aligned} \tag{11}$$

where the linear yarn density $\mu_\mathrm{F,yarn}$ and the fibre density ρ_F for the coincident axial and braid yarns are given in Table 6 and the intra-yarn and global FVFs are taken from Table 3.

For the longitudinal (x), transverse (y) and braid yarn direction ($1F$), the predicted elastic moduli are compared to their experimental equivalent as a function of the braiding angle θ in Fig. 20 (a). Error bars indicate one standard deviation for a total of six specimen tested. While the properties of the first two principal load directions (x and y) are directly calculated from homogenisation of the unit cell, the modulus in braid fibre direction ($1F$) is obtained by an additional rotation of the macroscopic in-plane stiffness tensor. Consequently, this orientation implicitly incorporates deviations of the shear modulus G_xy and the Poisson's ratio ν_xy.

Due to the higher degree of overall bundle distortion after compaction, the second nesting case consistently yields the lower stiffness among the two stacking configurations. However, the magnitude of this knock-down is comparably small, since the localised defects are smeared over a finite volume during the subsequent homogenisation step. Nonetheless, the effect on the non-linear response including failure is expected to be significantly larger [43, 44]. For the principal directions, the unit cell predictions match the experiments exceptionally well, with a maximum relative error of 3.4 % in the case of a [0/±30] braid loaded in x direction. A similar trend is encountered in case the applied load is aligned with the braid fibre direction $1F$, with the exception that the stiffness of the [0/±60] architecture is severely over-predicted with a relative error of 10.5 %. While this is the most pronounced case, the predictions generally exceed the experimental results. For minimised computational effort, we assume an infinite stack of plies in through-thickness direction and hence over-estimate their out-of-plane support in comparison to an actual braided laminate [43]. If we now directly introduce the load in the fibre direction of the heavily undulating braid bundles, local out-of-plane deformations develop as a result of non-zero bend-extension coupling terms accompanied by a degradation of the effective modulus E_1F.

Despite its relative simplicity, the elastic properties predicted by the analytical model match those of the unit cell very well. Clearly, the small improvements do not justify the extensive modelling effort and the computational cost associated with meso-scale unit cells. In case sufficient data on the detailed textile architecture is available, analytical models are well suited to predict the stiffness of the braided composites [45–47]. However, they do not provide localised stress-strain fields necessary for subsequent modelling of damage propagation.

Fig. 20 (b) completes the comparison of the elastic properties by a comprehensive summary of the in-plane Poisson's ratios. An excessive Poisson's effect in axial direction is encountered in the [0/±30] material. Here, the discrepancy of the longitudinal and transverse stiffness is most prominent. As the braiding angle increases, this mismatch becomes less pronounced, with a tendency towards a balanced Poisson's effect in the [0/±60] architecture. Up to a braiding angle of 45°, experiments and predictions differ by a magnitude comparable to the elastic moduli, with the sole exception of

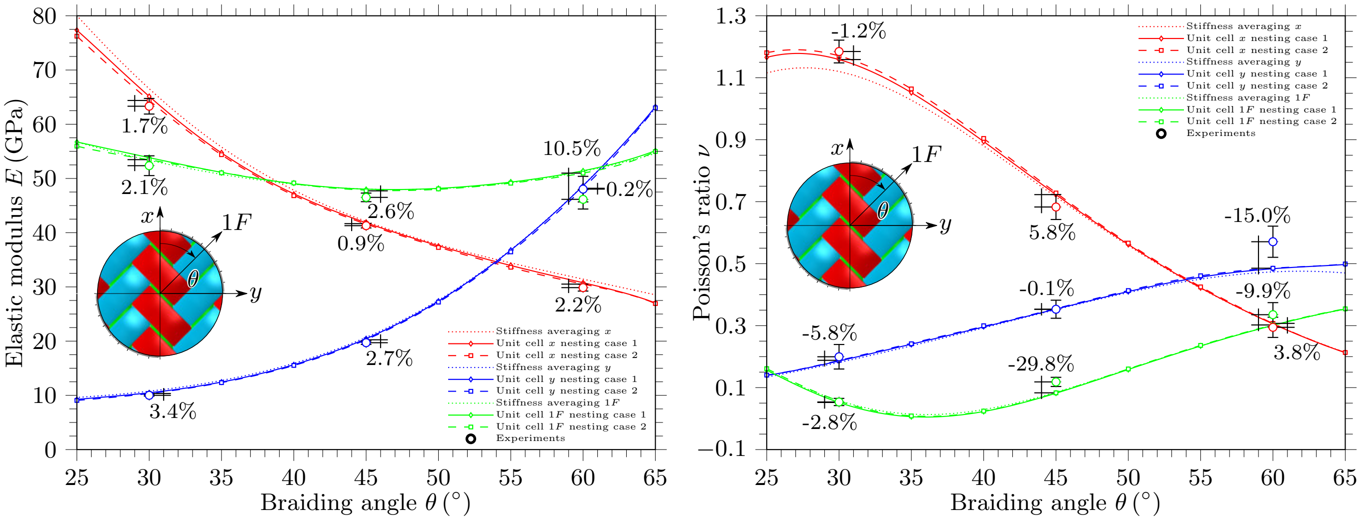

(a)

(b)

Figure 20: Comparison of homogenised experimental and predicted (a) elastic moduli (b) Poisson's ratios as a function of the braiding angle θ

the $1F$ direction. The corresponding jump of the relative error may be attributed to ν converging to a value close to zero. In the [0/±60] braid, the axial experiments are predicted well by the unit cell model. Contrarily, the remaining load cases exhibit a relative error up to 15 %, possibly originating from a larger mismatch between the unit cell and the actual internal geometry of the composite. Again, the differences between the unit cell and the stiffness averaging model predictions are small.

After having successfully demonstrated a minimal sensitivity of the simulated yarn path to the mesh cases under investigation, the preceding refinement study is extended to the stress fields inside the yarns. Coincident with the positions in Fig. 19, the stress distribution in the local braid fibre direction $\sigma_{1\mathrm{b}}$ is assessed as a result of the unit cell being subjected to a homogenised shear stress $\langle\tau_{\mathrm{xy}}\rangle$ in a linear analysis. For each mesh, the nominal stress is calculated at the centre and the side nodal position of the actual yarn path by extrapolation of the closest integration points. Hence, we benchmark the net effect of mesh refinement along the complete simulation chain, including both the geometric and actual mesh convergence. Fig. 21 (a) compares the linear stress concentration factor $\sigma_{1\mathrm{b}}/\langle\tau_{\mathrm{xy}}\rangle$ for different mesh densities along the top path of the braid bundles. Aside from the periodic pattern being represented well in all configurations, the element count in the yarn through-thickness direction outweighs the effect of global mesh refinement, particularly with regards to the peak amplitudes. When the bundle thickness is discretised with four elements, a global mesh refinement leads to a negligible change in the stress distribution compared to the medium case. Contrarily to the top position, the effect of a denser global mesh is more pronounced along the side of a braid bundle as shown in Fig. 21 (b). While both medium mesh cases yield comparable peak amplitudes here, the stress distribution along the yarn path tends to experience less noise and more distinct peaks with increasing refinement, as local bending effects are reproduced more accurately. Similar to the convergence behaviour during compaction and considering the additional computational expense of a fine mesh, a global mesh size of of $l_{\mathrm{mesh}} = 70\,\mu$m is deemed sufficient to capture local stresses accurately.

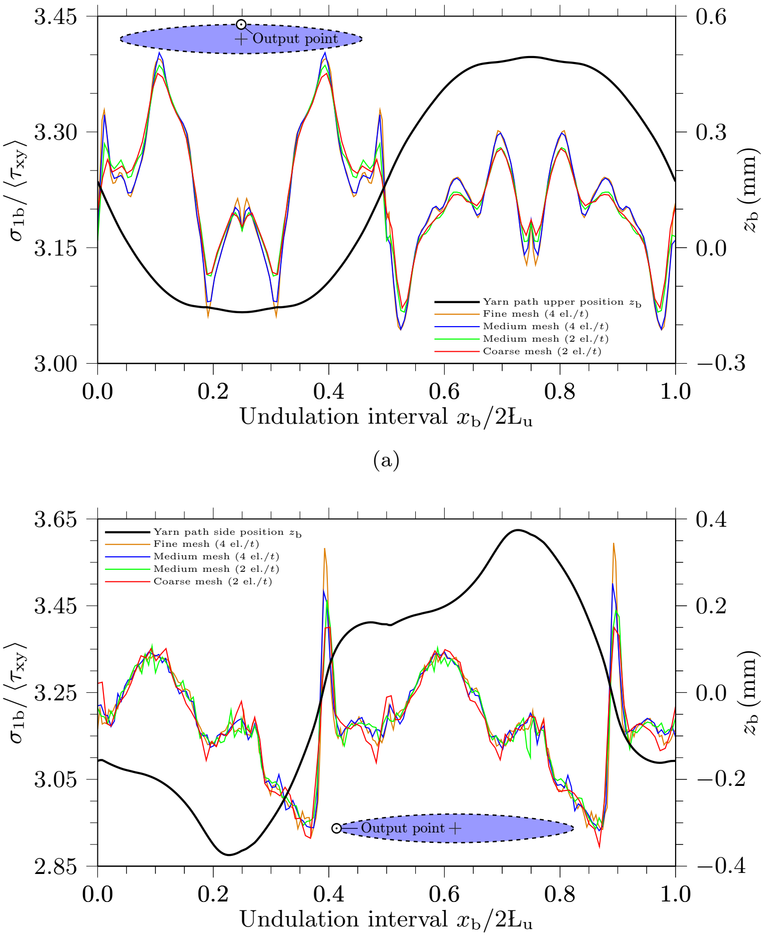

(a)

(b)

Figure 21: Effect of mesh density on the stress distribution in fibre direction along a single undulation interval (a) at the top position and (b) at the side of the braid bundles

4. Conclusion

In this paper, a novel simulation framework for accurate predictions of the the mechanical response of triaxial braided composites was proposed. Realistic FE unit cell models were generated through an automated bottom-up simulation work-flow: local volumetric interpenetrations present in the initial stage of the model were resolved in a fictitious thermal step. Subsequently, a compaction simulation was performed to the desired target fibre volume fraction using flexible membranes for improved computational efficiency. Special out-of-plane periodic boundary conditions allow an implicit consideration of the compaction of multiple braid plies in different nesting configurations which enabled us to capture global FVFs of 55 − 60% while using intra-yarn fibre volume fractions obtained from experiments. In the last step, a tetrahedral matrix pocket mesh was created from a CAD reconstruction of the deformed textile. A novel meshing methodology was developed to incorporate branching cohesive yarn-to-yarn and yarn-to matrix interfaces without the need of introducing an artificial matrix mesh of finite thickness. The framework was validated by detailed comparison with experimental results. First, the unit cell geometry was compared to the detailed reconstruction of the actual bundle geometry from μCT measurements for three braid architectures, with a nominal braiding angle of 30°, 45° and 60°. Subsequently, the predictive capability of the approach and its robustness were demonstrated by successfully generating models in an automatic fashion for braiding angles ranging from 25° to 65°. These models were successfully used to predict the elastic properties obtained experimentally. The excellent correlation of experiments and unit cell predictions underlines the framework's potential for future damage modelling.

Acknowledgements

This work was partially funded under the UK Engineering and Physical Sciences Research Council (EPSRC) Programme Grant EP/I02946X/1 on High Performance Ductile Composite Technology. The first author would like to acknowledge Bernhard Plank for the μCT measurements performed at the University of Applied Sciences Upper Austria, Thomas Hinterbrandner for the segmentation work and Dr. Jörg Cichosz for his valuable comments on this paper.

References

[1] Ayranci C, Carey J. 2d braided composites: A review for stiffness critical applications. Composite Structures 2008;85(1):43–58.

[2] Verpoest I, Lomov SV. Virtual textile composites software wisetex: Integration with micro-mechanical, permeability and structural analysis. Composites Science and Technology 2005;65:2563–74. 20th Anniversary Special Issue.

[3] Long A, Brown L. 8 - modelling the geometry of textile reinforcements for composites: Texgen. In: Boisse P, editor. Composite Reinforcements for Optimum Performance. Woodhead Publishing Series in Composites Science and Engineering; Woodhead Publishing. ISBN 978-1-84569-965-9; 2011, p. 239–64.

[4] Lomov SV, Ivanov DS, Verpoest I, Zako M, Kurashiki T, Nakai H, et al. Meso-fe modelling of textile composites: Road map, data flow and algorithms. Composites Science and Technology 2007;67(9):1870–91.

[5] Hsu SY. Literature reviews on modeling internal geometry of textile composites and rate-independent continuum damage. Tech. Rep. NASA/TM-2011-217079; NASA Langley Research Center, Hampton, VA, United States; 2011.

[6] Hivet G, Boisse P. Consistent mesoscopic mechanical behaviour model for woven composite reinforcements in biaxial tension. Composites Part B: Engineering 2008;39(2):345–61.

[7] Nguyen Q, Vidal-Sall E, Boisse P, Park C, Saouab A, Brard J, et al. Mesoscopic scale analyses of textile composite reinforcement compaction. Composites Part B: Engineering 2013;44(1):231–41.

[8] Grail G, Hirsekorn M, Wendling A, Hivet G, Hambli R. Consistent finite element mesh generation for meso-scale modeling of textile composites with preformed and compacted reinforcements. Composites Part A: Applied Science and Manufacturing 2013;55(0):143–51.

[9] Said BE, Green S, Hallett SR. Kinematic modelling of 3d woven fabric deformation for structural scale features. Composites Part A: Applied Science and Manufacturing 2014;57(0):95–107.

[10] Zhou G, Sun X, Wang Y. Multi-chain digital element analysis in textile mechanics. Composites Science and Technology 2004;64(2):239–44.

[11] Green S, Matveev M, Long A, Ivanov D, Hallett S. Mechanical modelling of 3d woven composites considering realistic unit cell geometry. Composite Structures 2014;118(0):284–93.

[12] Doitrand A, Fagiano C, Irisarri FX, Hirsekorn M. Comparison between voxel and consistent meso-scale models of woven composites. Composites Part A: Applied Science and Manufacturing 2015;73(0):143–54.

[13] Potter E, Pinho S, Robinson P, Iannucci L, McMillan A. Mesh generation and geometrical modelling of 3D woven composites with variable tow cross-sections. Computational Materials Science 2012;51(1):103–11.

[14] Naouar N, Vidal-Sallé E, Schneider J, Maire E, Boisse P. Meso-scale fe analyses of textile composite reinforcement deformation based on x-ray computed tomography. Composite Structures 2014;116(0):165–76.

[15] Faes J, Rezaei A, Van Paepegem W, Degrieck J. Accuracy of 2d fe models for prediction of crack initiation in nested textile composites with inhomogeneous intra-yarn fiber volume fractions. Composite Structures 2016;140:11–20.

[16] Carvalho ND, Pinho S, Robinson P. Reducing the domain in the mechanical analysis of periodic structures, with application to woven composites. Composites Science and Technology 2011;71(7):969–79.

[17] Tang X, Whitcomb JD. General techniques for exploiting periodicity and symmetries in micromechanics analysis of textile composites. Journal of Composite Materials 2003;37(13):1167–89.

[18] Sevenois R, Garoz D, Gilabert F, Spronk S, Fonteyn S, Heyndrickx M, et al. Avoiding interpenetrations and the importance of nesting in analytic geometry construction for representative unit cells of woven composite laminates. Composites Science and Technology 2016;136:119–32.

[19] Melro A, Camanho P, Andrade Pires F, Pinho S. Numerical simulation of the non-linear deformation of 5-harness satin weaves. Computational Materials Science 2012;61:116–26.

[20] Römelt P, Cunningham P. A multi-scale finite element approach for modelling damage progression in woven composite structures. Composite Structures 2012;94(3):977–86.

[21] Carvalho ND, Pinho S, Robinson P. Numerical modelling of woven composites: Biaxial loading. Composites Part A: Applied Science and Manufacturing 2012;43(8):1326–37.

[22] Jacques S, Baere ID, Paepegem WV. Application of periodic boundary conditions on multiple part finite element meshes for the meso-scale homogenization of textile fabric composites. Composites Science and Technology 2014;92(Supplement C):41 – 54.

[23] Ivanov DS, Baudry F, Van Den Broucke B, Lomov SV, Xie H, Verpoest I. Failure analysis of triaxial braided composite. Composites Science and Technology 2009;69(9):1372–80.

[24] Zhang C, Binienda WK, Goldberg RK, Kohlman LW. Meso-scale failure modeling of single layer triaxial braided composite using finite element method. Composites Part A: Applied Science and Manufacturing 2014;58:36–46.

[25] Pinho S, Darvizeh R, Robinson P, Schuecker C, Camanho P. Material and structural response of polymer-matrix fibre-reinforced composites. Journal of Composite Materials 2012;46(19-20):2313–41.

[26] Abaqus Documentation. Dassault Systèmes Simulia Corp., Providence, RI, USA; 2014.

[27] Melenka G, Hunt A, van Ravenhorst J, Akkerman R, Pastore C, Ko F, et al. 3 - manufacturing processes for braided composite materials. In: Carey JP, editor. Handbook of Advances in Braided Composite Materials. Woodhead Publishing. ISBN 978-0-08-100369-5; 2017, p. 47 – 153.

[28] Hans T, Cichosz J, Brand M, Hinterhölzl R. Finite element simulation of the braiding process for arbitrary mandrel shapes. Composites Part A: Applied Science and Manufacturing 2015;77:124 –32.

[29] Tang X, Whitcomb JD, Kelkar AD, Tate J. Progressive failure analysis of 2x2 braided composites exhibiting multiscale heterogeneity. Composites Science and Technology 2006;66(14):2580–90.

[30] Bažant ZP, Oh BH. Crack band theory for fracture of concrete. Matériaux et Construction 1983;16(3):155–77.

[31] Endruweit A, Long A. A model for the in-plane permeability of triaxially braided reinforcements. Composites Part A: Applied Science and Manufacturing 2011;42(2):165–72.

[32] Boisse P, Gasser A, Hagege B, Billoet JL. Analysis of the mechanical behavior of woven fibrous material using virtual tests at the unit cell level. Journal of Materials Science 2005;40(22):5955–62.

[33] Badel P, Vidal-Sallé E, Maire E, Boisse P. Simulation and tomography analysis of textile composite reinforcement deformation at the mesoscopic scale. Composites Science and Technology 2008;68(12):2433–40.

[34] Doitrand A, Fagiano C, Chiaruttini V, Leroy F, Mavel A, Hirsekorn M. Experimental characterization and numerical modeling of damage at the mesoscopic scale of woven polymer matrix composites under quasi-static tensile loading. Composites Science and Technology 2015;119:1–11.

[35] Birkefeld K, Röder M, von Reden T, Bulat M, Drechsler K. Characterization of biaxial and triaxial braids: Fiber architecture and mechanical properties. Applied Composite Materials 2012;19(3):259–73.

[36] Cichosz J, Wehrkamp-Richter T, Körber H, Hinterhölzl R, Camanho PP. Failure and damage characterization of (±30°) biaxial braided composites under multiaxial stress states. Composites Part A: Applied Science and Manufacturing 2016;90:748–59.

[37] Wehrkamp-Richter T, Hinterhölzl R, Pinho ST. Damage and failure of triaxial braided composites under multiaxial stress states. Composites Science and Technology 2017;150:32–44.

[38] ASTM International . ASTM D3039 - Standard Test Method for Tensile Properties of Polymer Matrix Composite Materials. 2008.

[39] Weissenböck J, Bhattacharya A, Plank B, Heinzl C, Kastner J. Visual classification of braided and woven fiber bundles in x-ray computed tomography scanned carbon fiber reinforced polymer specimens. Case Studies in Nondestructive Testing and Evaluation 2016;.

[40] ASTM International . ASTM D3171 - Standard Test Methods for Constituent Content of Composite Materials. 2009.

[41] Chamis CC. Simplified composite micromechanics equations for strength, fracture toughness, impact resistance and environmental effects. Tech. Rep.; NASA Technical Memorandum 83696; 1984.

[42] Quek SC, Waas AM, Shahwan KW, Agaram V. Analysis of 2d triaxial flat braided textile composites. International Journal of Mechanical Sciences 2003;45(6-7):1077 –96.

[43] Ivanov DS, Lomov SV, Ivanov SG, Verpoest I. Stress distribution in outer and inner plies of textile laminates and novel boundary conditions for unit cell analysis. Composites Part A: Applied Science and Manufacturing 2010;41(4):571–80.

[44] Doitrand A, Fagiano C, Leroy FH, Mavel A, Hirsekorn M. On the influence of fabric layer shifts on the strain distributions in a multi-layer woven composite. Composite Structures 2016;145:15–25.

[45] Gommers B, Verpoest I, Houtte PV. The moritanaka method applied to textile composite materials. Acta Materialia 1998;46(6):2223 –35.

[46] Byun JH. The analytical characterization of 2-d braided textile composites. Composites Science and Technology 2000;60(5):705 –16.

[47] Potluri P, Manan A, Francke M, Day R. Flexural and torsional behaviour of biaxial and triaxial braided composite structures. Composite Structures 2006;75(1-4):377–86.